Phase transitions in 2D materials

Wenbin Li[1]✉, *Xiaofeng Qian*[2] *and Ju Li*[3]✉

Abstract | The discovery and control of new phases of matter is a central endeavour in materials research. The emergence of atomically thin 2D materials, such as transition-metal dichalcogenides and monochalcogenides, has allowed the study of diffusive, displacive and quantum phase transitions in 2D. In this Review, we discuss the thermodynamic and kinetic features of 2D phase transitions arising from dimensionality confinement, elasticity, electrostatics, defects and chemistry unique to 2D materials. We highlight polymorphic, ferroic and high-temperature diffusive phase changes, and examine the technological potential of controlled 2D phase transitions. Finally, we give an outlook to future opportunities in the study and applications of 2D phase transitions, and identify key challenges that remain to be addressed.

Self-organization of a large number of nuclides and electrons leads to the emergence of different phases of matter. A phase represents a certain style of organization that can be spatially replicated ad infinitum, with properties that change continuously in response to external fields, that are distinct from the other phases. Therefore, certain system properties are altered as the material undergoes a phase transition. A general characteristic of a phase transition is that it either involves a discontinuity in an order parameter according to the Landau paradigm of phase transitions[1–3] or a change in a topological invariant[4,5].

The discovery, characterization and control of different phases of matter is a central task in condensed matter physics and materials science. In particular, the study of phase transitions in 2D systems has played a crucial role in advancing our understanding of phase transitions (FIG. 1). 2D materials[6–10] are matter that can infinitely replicate in two directions but have thickness at the atomic level in the third direction. For example, monolayer MoS_2 has a thickness of 6.7 Å and is typically micrometres in-plane in laboratory samples produced by mechanical exfoliation[6], thus, possessing an aspect ratio of ~10^3 or more. For comparison, a typical piece of A4-sized paper (~100 μm × 29.7 cm × 21 cm) would have a similar aspect ratio of ~10^3. Although 2D↔3D/1D phase transitions are certainly interesting subjects of discussion, here, we focus on 2D→2D transitions.

The earliest studies of 2D phase transitions were mostly theoretical; for example, the exact solution of the 2D Ising spin model[11], the proposition of the Hohenberg–Mermin–Wagner theorem[12,13] and the discovery of the Kosterlitz–Thouless transition[14,15] (FIG. 1). In the early 1980s, progress in semiconductor technology allowed the experimental study of 2D electron systems confined at semiconductor interfaces and under intense magnetic fields, which led to the ground-breaking discovery of the quantum Hall effect (QHE)[16] and the fractional quantum Hall effect (FQHE)[17]. The invention of the scanning tunnelling microscope (STM)[18] and the atomic force microscope (AFM)[19] in the 1980s enabled real-space imaging of surface reconstruction[20,21] and of the phase transformation of Langmuir monolayers[22]. Techniques for isolating planar sheets of crystals from their bulk counterparts only became available in the early 2000s[6,23], paving the way for experimental studies of phase transitions in free-standing 2D materials. A wide range of phase transitions have been explored in 2D materials, including quantum electronic phase transitions, such as QHE[24], FQHE[25,26], metal–insulator transitions[27], superconductivity[28–30], the quantum spin Hall (QSH) effect[31–35], the quantum anomalous Hall (QAH) effect[36–38], magnetic phase transitions[39–45] and classical phase transitions, such as polymorphic phase transitions[46–54] and ferroic phase transitions[55–59] (FIG. 1).

The reduction in dimensionality from 3D to 2D leads to peculiar statistical physics (for example, melting and critical point behaviours), quantum physics (for example, quantum confinement) and mechanics (for example, out-of-plane bending and buckling), and makes 2D systems more sensitive to the ambient chemical environment (for example, adsorption and corrosion), external fields and physical contacts. Indeed, investigating 2D materials could be regarded as the ultimate 'surface science', because all effects are happening on or near the surface. From an engineering perspective, this creates both opportunities and challenges for controlling and using phase change in 2D. For example, an optomechanical phase change[59,60] is easier to induce in free-standing 2D materials, owing to less elastic confinement and strong light–matter interactions in 2D compared with 3D bulk. However, air stability and chemical purity become bigger issues in 2D and influence the phase-change behaviour.

[1]*School of Engineering and Key Laboratory of 3D Micro/Nano Fabrication and Characterization of Zhejiang Province, Westlake University, Hangzhou, China.*

[2]*Department of Materials Science and Engineering, Texas A&M University, College Station, TX, USA.*

[3]*Department of Nuclear Science and Engineering and Department of Materials Science and Engineering, Massachusetts Institute of Technology, Cambridge, MA, USA.*

✉*e-mail: liwenbin@westlake.edu.cn; liju@mit.edu*

https://doi.org/10.1038/s41578-021-00304-0

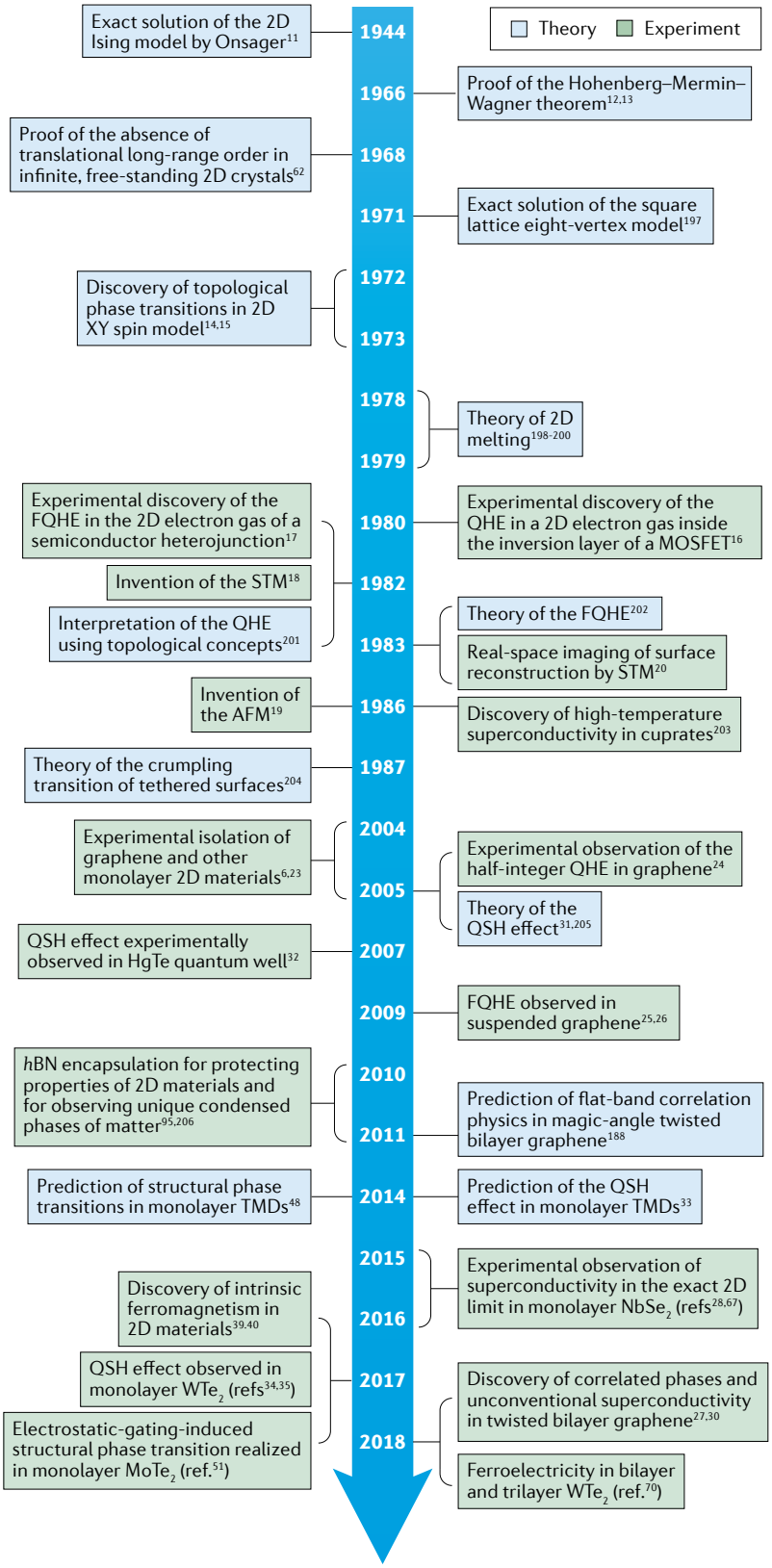

Fig. 1 | **Timeline of key developments in the study of 2D phase transitions.** AFM, atomic force microscope; FQHE, fractional quantum Hall effect; *h*BN, hexagonal boron nitride; MOSFET, metal–oxide–semiconductor field-effect transistor; QHE, quantum Hall effect; QSH, quantum spin Hall; STM, scanning tunnelling microscope; TMD, transition-metal dichalcogenide.

Prior to the emergence of free-standing 2D materials, extended defects in 3D material hosts, such as stacking faults, surfaces, grain boundaries and phase boundaries, have been considered 2D 'phases' in contact with 3D phase(s), on either side or both sides of the 2D plane. Thermodynamic and kinetic features, such as interfacial segregation, pre-melting[61] and glissile versus diffusive reconstruction, are analogous to phase transitions in free-standing 2D materials. Therefore, surface and interfacial science shares many features with 2D materials science and, aside from different long-range elastic and electrostatic energy expressions, many surface/interfacial phase transitions are similar to phase transitions in 2D materials.

In this Review, we outline unique features of phase transitions that emerge in 2D materials and highlight recent key studies of 2D material phase transitions and technological implications of 2D phase changes. We will also provide an outlook to future opportunities of phase transformations in 2D materials.

Unique features of 2D phase transitions

Dimensionality (D) reduction can strongly affect internal interactions and statistical physics, and, thus, the behaviour of phase transitions. In 1968, Mermin showed that thermal fluctuations destroy the long-range diffraction order of infinite, free-standing 2D crystals[62]. Similarly, in 1D polymers, the preferred stress-free configuration at finite temperature is a 'globule of yarn' with an end-to-end distance of $\propto N^{1/2}$, where N is the contour length, caused by conformational entropy. A completely unconstrained 2D material cannot maintain its flatness in a 3D space and would prefer to adopt the configuration of a 'paper ball'. In contrast with 3D crystals or liquids, which can sustain static compression, free-standing 2D crystals cannot sustain static compression even at zero temperature, owing to long-wavelength Euler-buckling-like instability, which occurs at arbitrarily small compressive stress for infinite crystals. Thus, 1D and 2D crystals are more fragile than 3D crystals in the statistical physics sense, shown by the Hohenberg–Mermin–Wagner theorem[12,13] for systems with sufficiently short-range interactions in $D \leq 2$. In reality, most 2D crystals are not completely free and are constrained either on the bottom by a substrate through adhesion and friction forces or at the ends, preventing thermal fluctuations from destroying the flatness of the material. Nonetheless, out-of-plane flexural vulnerabilities are intrinsic to any 2D material and, when coupled with external stimuli locally or globally, they can give rise to a variety of interesting behaviours.

The effect of dimensionality can be understood in terms of short-range and long-range interactions. Short-range effects mainly occur in the form of coordination number and symmetry of chemical bonding, whereas long-range interactions can be much longer than the interatomic distance and include electrostatic, magnetostatic and elastic interactions. Both short-range and long-range interactions can undergo substantial

changes going from $D = 3$ to $D = 2$. In addition, the 2D nature of these materials facilitates coupling between the system and the environment, leading to higher susceptibility of phase stability to external stimuli.

Short-range interactions

Dimensionality reduction gives rise to the loss of coordination number, causing rehybridization of valence electrons (for example, competition between sp^3 and sp^2 hybridization in carbonaceous materials) that can shift the energetic order of phases and cause the emergence of new symmetries. In 2D surfaces, which we have argued to be analogous to 2D materials, cutting off one half of the bulk necessitates the breaking of strong bonding interactions, such as metallic, covalent or ionic bonds in the vertical direction, which can lead to the surface reconstruction of certain inorganic materials, such as the 7×7 reconstruction on the (111) surface of silicon[20]. Indeed, surface reconstruction can be considered a 2D phase transition.

If a 2D material is exfoliated from the bulk through the removal of weak interactions, for example, in many-layered 3D crystals, in which interlayer interaction is predominantly of the van der Waals type, short-range coordination and symmetry can still be affected. In this case, electron–phonon interactions can change through confinement-induced modifications in the electronic structure[63,64], vibrational spectrum[65] or dielectric environment[66]. Owing to the small thickness of 2D materials, dielectric screening normal to the layer is limited; a 2D material in the out-of-plane direction resembles a molecule surrounded by vacuum. Therefore, the electrostatic potential generated by lattice vibrations in 2D materials is less screened than in 3D bulk materials, which increases the strength of electron–phonon interactions. Consequently, 2D materials are more susceptible to charge density wave and Peierls distortions[67], lattice instabilities (FIG. 2a) that can considerably alter the short-range coordination and bonding symmetry.

Long-range interactions

Long-range interactions in 2D materials, such as electrostatic and elastic interactions, are also fundamentally different from their counterparts in 3D bulk materials (FIG. 2b). The dielectric property of a suspended, isolated 2D material is analogous to that of a layer of molecules, owing to weak dielectric screening in the out-of-plane direction. In the in-plane directions,

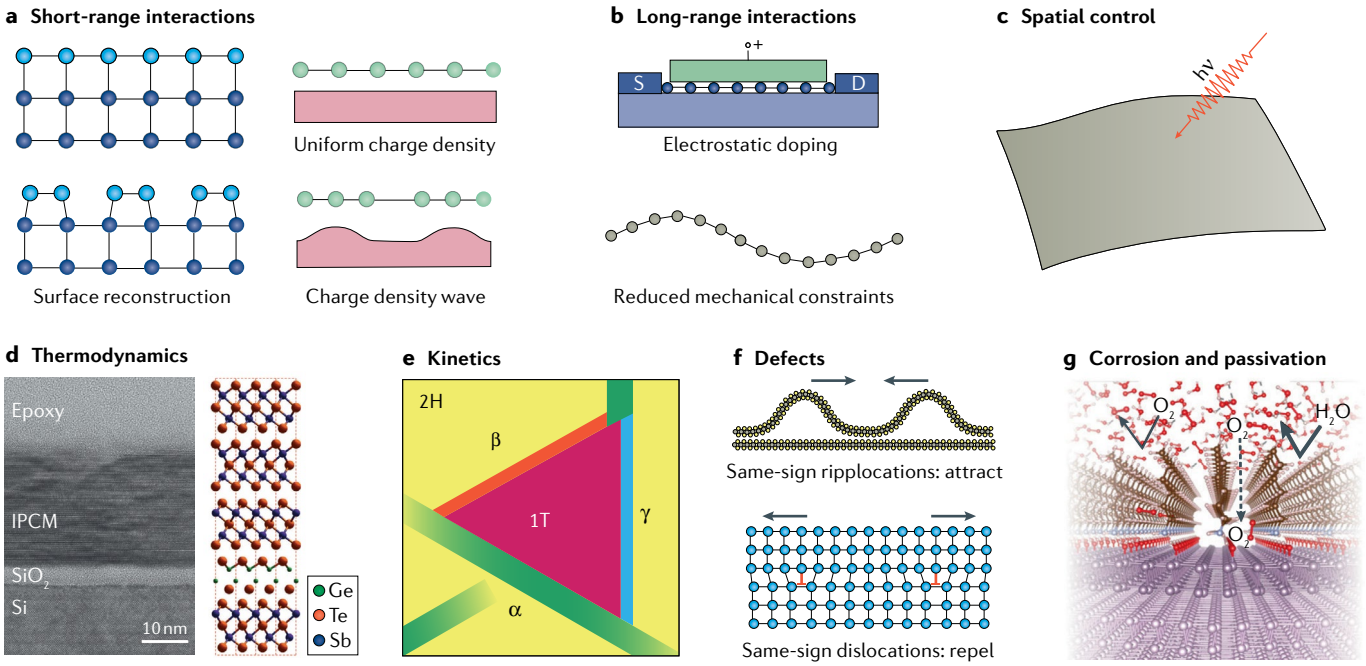

Fig. 2 | **Distinct features of phase transitions in 2D materials.** **a** | Short-range interactions. Dimensionality reduction causes the breaking of chemical bonds, which can lead to 2D structural transformations, such as surface reconstruction of inorganic materials. Dimensionality confinement can also cause an increase in charge density wave instability and Peierls distortion, which are short-range lattice instabilities owing to electron–phonon interactions. **b** | Long-range interactions. Weak dielectric screening in the out-of-plane direction enables electrostatic doping of 2D materials to achieve high carrier densities. In addition, mechanical constraints are reduced in 2D materials, owing to the volumetric nature of the strain energy and the low energy cost of forming ripples. **c** | Spatial addressability allows coupling with external stimuli and the precise local control of phase transitions. **d** | The thermodynamics of 2D phase transitions are illustrated in interfacial phase-change materials (IPCM). A transmission electron micrograph and atomistic model of $(GeTe)_2(Sb_2Te_3)_4$ are shown[81]. Confined atomic motion results in low volume and small entropy loss per volume, and, thus, low switching energy. **e** | Phase transformation kinetics are illustrated by the 2H-to-1T phase transition of monolayer MoS_2 (REF.[76]). Intermediate phases (α, β and γ) are formed prior to the transformation from the 2H to the 1T phase. **f** | Defects, such as ripplocations, can form in 2D materials during phase transition[73], which attract each other when close in distance; by contrast, same-sign dislocations in 3D repel each other. **g** | The atomic thickness and poor environmental stability of 2D materials require new passivation strategies against corrosion, for example, coating with waterproof monolayers to prevent the oxidation–dissolution cycle in corrosion. Panel **d** reprinted from REF.[81], Springer Nature Limited. Panel **e** adapted from REF.[76], Springer Nature Limited. Panel **f** adapted with permission from REF.[73], American Chemical Society. Panel **g** reprinted with permission from REF.[97], National Academy of Sciences.

the Coulomb potential cannot be effectively screened at the long-wavelength limit either, given that most of the electric field lines associated with spatially separated charges would reside in the vacuum region and not pass through the 2D material[65]. Therefore, the macroscopic dielectric screening in a 2D insulator is not characterized by a simple dielectric constant tensor as in the 3D crystal but is intrinsically dependent on the wavevector $\boldsymbol{q}$. At the long-wavelength limit, the in-plane dielectric function of an isotropic 2D dielectric can be written as $\varepsilon(\boldsymbol{q}_{\parallel}) = 1 + 2\pi\alpha_{2D}|\boldsymbol{q}_{\parallel}|$, where $\boldsymbol{q}_{\parallel}$ is the in-plane wavevector and α_{2D} is the polarizability of the 2D dielectric sheet[66]. At the limit of $\boldsymbol{q}_{\parallel}$ approaching zero, the value of the dielectric function reaches the vacuum value of unity, which means that the Coulomb potential becomes essentially unscreened.

The weakened dielectric screening in 2D materials has a range of consequences for phase transitions. In addition to the aforementioned charge density wave and Peierls instabilities, which can arise from enhanced electron–phonon interactions, because the thickness of 2D materials is typically smaller than the Debye screening length, 2D materials can be electrostatically doped. A high carrier density of up to $10^{14}\,e\,\mathrm{cm}^{-2}$ can be achieved by applying a gate voltage in the out-of-plane direction[68]. Such electrostatic doping is not possible in 3D materials, because a net positive charge density ρ ($e\,\mathrm{cm}^{-3}$) in 3D bulk must lead to the divergence of the cohesive energy per atom, also called 3D Coulomb explosion. In contrast, electrostatic doping of a 2D sheet ($e\,\mathrm{cm}^{-2}$) in contact with a 3D electrode is energetically feasible and provides a versatile tool to control carrier density and phase transitions in 2D, as long as there are compensating charges outside of the plane (electrical double layer). Indeed, electrostatic doping has been employed to study 2D phase transitions, including classical[51] and quantum[27,68,69] phase transitions. Remarkably, owing to restricted dielectric screening in the out-of-plane direction, 2D metals, such as few-layer WTe_2 and graphene, can also exhibit ferroelectricity[70,71] or flexoelectricity[72]. Here, the out-of-plane polarity can be switched by an electric field (ferroelectricity) or generated by a strain gradient or a bending curvature[72] (flexoelectricity). Such macroscopic polarization is not possible in a 3D metal, because electric polarization will be fully screened by free electrons.

Elastic interaction, which is an important long-range interaction in classical phase transition theory, is fundamentally altered when going from $D = 3$ to $D = 2$ (REF.[73]). 2D materials, such as graphene and transition-metal dichalcogenides, exist in a 3D space and, thus, can bend out-of-plane. In-plane compression triggers buckling instability and, therefore, only positive in-plane stress (tension) can exist along any of the two principal axes of a homogeneous stress field. In addition, owing to a lack of constraint in the z-direction, the elastic energy penalty along a phase transformation pathway is less significant than in 3D, in particular, if the membrane is slightly pre-compressed[59]. It is known from physical metallurgy that long-range elastic energy often competes with short-range interfacial energy in determining the dominant length scale in microstructures, for example, the characteristic twin thickness of lath martensites in steel. The replacement of long-range elastic energy by shorter-range elastic bending energy[73] and van der Waals adhesion energy fundamentally alters the energy landscape of phase transitions in 2D crystals, as compared with bulk 3D crystals, leading to faster transitions[59,60] with a lower nucleation energy barrier.

Spatial control

An important feature of 2D materials is that all atoms are either located on the surface or a few Ångstroms away from the surface. Thus, the atoms in 2D materials are more exposed to the environment than in 3D materials. This, in conjunction with internal electronic structure properties, such as van Hove singularities in the electronic density of states[74], leads to enhanced coupling with external fields, such as electromagnetic waves of a certain frequency (FIG. 2c). Electric fields can penetrate through 2D semiconductors and insulators, owing to their atomic thickness and restricted dielectric screening[52]. Based on this, electrostatic doping can uniformly or heterogeneously ('charge puddles') control the carrier density of the material[68], and laser and focused electron beams can induce phase transitions at distinct locations[50]. Moreover, adsorbates can cover the surface and induce phase transformations[75]. The possibility of spatially controlled induction of phase transitions by external stimuli also allows atomic-level visualization of the phase transformation process by transmission electron microscopy (TEM)[76].

Optical or electrical readouts are often sensitive enough to locate 2D materials or to detect monolayer-scale changes: consider, for example, Benjamin Franklin's famed experiment at Clapham Common pond that described the swift spread of oil on water[77]. Lord Rayleigh carried out a similar experiment about a century later and calculated, for the first time, the thickness of an oleic acid monolayer[78]. Monolayer graphene can also be visually detected by the naked eye because it absorbs 2.3% of light[79] — the physical basis of the Scotch tape method of 2D sample preparation[6,23].

Thermodynamics

The free energy needed to drive a phase transition is a crucial factor for the application of phase-change materials. A first-order phase transition involves latent heat that originates from a discontinuity in entropy. The latent heat L is given by $L = T\Delta S$, where T is the transition temperature and ΔS is the difference in entropy between higher-entropy and lower-entropy phases. For a classical solid-to-solid diffusionless phase transition, the entropy difference ΔS mainly arises from a variation in the vibrational, electronic and/or magnetic entropy between two phases, whereas for a phase transition that involves a liquid or gas phase, a change in configurational entropy often dominates. Entropy is an extensive quantity and, thus, the volume reduction associated with a dimensionality change from 3D to 2D can lead to a substantial decrease in latent heat. Therefore, in most cases, much less energy is required to induce a readable phase change in 2D materials compared with 3D materials.

Latent heat can be supplied either through contact with a heat bath or by dissipative processes, such as

Joule heating. In the general case that external work is also involved in driving a first-order phase transition, the total external energy supply can be determined by the fundamental thermodynamic relation $dU = T\,dS + \sum_i Y_i dX_i$, where Y_i represents a generalized force and X_i represents the corresponding generalized displacement. For example, for a 2D structural phase transition induced by electrostatic gating[80], Y_i and X_i take the form of voltage V and total charge Q, respectively. Both X_i and S are extensive quantities and, therefore, dimensionality reduction can result in a considerable reduction in the external energy input.

In addition to the volumetric effect, dimensional confinement can also decrease the entropy difference per volume. For a phase transition that involves substantial configurational entropy variation, for example, a melting transition or order-to-disorder solid-state transformation, such a reduction of entropy difference per volume occurs if the 2D material is confined in a heterostructure setup, spatially restricting out-of-plane atomic motion. Confined atomic movement reduces the phase space available for thermal excitation, causing entropy loss. Therefore, interfacial phase-change materials[81], such as GeTe/Sb_2Te_3 superlattices, require considerably less switching energy than bulk $Ge_2Sb_2Te_5$ alloys, owing to melting-free switching in the confined GeTe layers, which occurs through the local atomic displacements of only the Ge atoms (FIG. 2d).

Transformation kinetics and defects

A first-order classical phase transition that entails a discontinuous change in the order parameter necessarily involves the nucleation and growth of a new phase. The kinetics of nucleation and growth are both substantially affected by D. For example, given that a first-order phase transition involves latent heat, the thermal conductivity of 2D materials, which depends on the dimensionality[82], affects the growth kinetics. Whether the 2D material is on a 3D substrate or not can also matter. In addition, the atomic vibrational frequency, the reaction coordinate of unit processes and the energy barrier for atomic rearrangements control the transformation kinetics and depend on dimensionality. Phase boundaries and domain walls in 2D materials are quasi-1D objects, in contrast with the 2D nature of phase and domain boundaries in bulk materials. In particular, the great reduction of elastic energy constraints in 2D materials facilitates displacive phase transitions with glissile transformation interfaces. For example, an in situ TEM study of the phase transition between two structural polymorphs of monolayer MoS_2 showed that the transformation between the semiconducting (2H) and metallic (1T) phases involves the initial formation of an intermediate phase and subsequent gliding of atomic planes of sulfur and molybdenum within a single layer[76] (FIG. 2e), which has very little elastic energy penalty, especially if the 2D membrane is slightly pre-compressed[59], that is, given some 'slack'.

Defects are the essential facilitators and by-products of phase transitions, and can also serve as preferred nucleation sites for new phases. In 2D materials, the physics and mechanics of defect nucleation and propagation are different than in 3D systems[83,84], leading to distinct defect population dynamics and inelastic relaxation mechanisms; namely, while the mechanical strength of large-volume 3D bulk materials is mainly controlled by the propagation of existing glissile defects, such as dislocations and cracks, the plastic flow or fracture strength of 2D materials are often controlled by defect nucleation. For example, while there are glissile dislocations in 2D materials, such as the pentagon–heptagon defect in graphene[85], there is no equivalence of the Frank–Read dislocation source in 3D materials. These factors enable 2D materials to withstand higher elastic strain before irreversible strain-energy relaxation processes occur, such as fracture and plasticity, as compared with 3D materials[84]. For example, experimentally confirmed tensile elastic strain limits of graphene and MoS_2 monolayers can be as high as 20% and 10%, respectively[86,87]. In contrast, the elastic strain limit of many bulk inorganic materials is typically only ~0.2%, indicating that a substantially larger strain space becomes available for controlling the physical properties and phase transitions of 2D materials. Thus, elastic strain engineering[88] and inelastic strain engineering of 2D materials are experimentally more feasible than in 3D bulk materials, owing to the higher tolerance of 2D materials to residual tensile and shear stresses before inelastic deformation occurs, such as plasticity, creep, damage or fracture. Large-tensile-strain-induced phase transitions have been theoretically[48] and experimentally[89,90] demonstrated in 2D materials.

2D materials placed on curved surfaces of 3D materials also show defect mechanics distinct from 3D materials. For example, in 2D crystals self-assembled on the surface of liquid droplets, the spatial curvature of the droplets can lead to the free termination of grain boundaries in the crystal, resulting in a disclination monopole[91]. The disclination monopole is energetically too expensive to form in 3D bulk crystals and, therefore, grain boundaries in 3D bulk must terminate at triple junctions connected to other grain boundaries, which is not necessarily the case in 2D materials with 3D curvature.

Corrosion and passivation

Environmental stability is crucial for the practical usage of 2D materials. Chemical complexity and thermochemical stability issues are already well known for grain boundaries and surfaces, as reflected by the Langmuir–McLean and Fowler–Guggenheim isotherms[92]. Generally speaking, if one regards surfaces and grain boundaries as 2D phases (embedded in a 3D phase), they have different equilibrium chemistries, as exemplified by interfacial segregation and the Gibbs adsorption isotherm, and, also, thermochemical or electrochemical stability windows different from the 3D host phase; thus, they can undergo phase transitions even when the 3D host does not, when an intensive thermodynamic variable (for example, temperature T, stress σ, voltage U) is varied. Corrosion, which is the degradation of materials in a chemical environment, could be considered a phase transition.

Many 2D crystals corrode in air, and, with the exception of graphene, almost all metallic 2D materials have air stability problems[93], even at room temperature.

For many 3D materials, the air stability problem is circumvented by the formation of a surface passivation layer; for example, a 2–5-nm stable layer of alumina that protects the material is formed if aluminium is exposed to the air. Here, passivation layers would only make up a small fraction of the otherwise unreacted bulk material. By contrast, the thickness of 2D materials is comparable or even smaller than that of passivation layers, making their passivation challenging. The corrosion of materials depends on the availability of oxygen (O_2) and water (H_2O) or hydrogen (H_2). By changing the partial pressure of O_2 or H_2, the redox potential and chemical transformation can be controlled, illustrated in the Pourbaix diagram[94], which is a chemical or electrochemical phase diagram. A boundary line in the Pourbaix diagram corresponds to a chemical transformation induced by the environment and the redox potential. Most 2D materials cannot form a natural passivation layer from their own reaction products and, therefore, strategies are required to restrict the contact of the material with O_2 and H_2O and to prevent the oxidation–dissolution cycle of corrosion. For example, environmentally fragile 2D materials can be covered with more robust materials, such as graphene or hexagonal boron nitride[95,96], or coated with water-repelling molecular monolayers, such as linear alkylamines[97].

New phase engineering concepts

The unique features of 2D phase transitions have led to new concepts for engineering the phases and properties of 2D materials. For example, the possibility of precise spatial addressability (as 2D locating is much easier than 3D locating), strong coupling with light and the propensity for displacive phase transitions enable optomechanical switching. Here, a laser beam is used to induce ultrafast, diffusionless, order-to-order phase transitions in 2D materials with degenerate ground states[59]. The large tensile elastic strain limit of 2D materials allows the imposition of a large elastic strain tensor for tuning the electrical[98], optical[99] and catalytic[100] properties of 2D materials, and for controlling their phase transitions[88]. 2D materials cannot sustain compressive strain and they have less constraints for structural relaxation in the layer-normal direction, as compared with 3D materials. Therefore, compressive strain can lead to the formation of ripplocations[73] (FIG. 2f), which are line defects that play an important role in the deformation of layered materials. Furthermore, the atomic-level thickness of 2D materials and their weak environmental stability have led to the development of new protection strategies, such as coating with molecular layers on 2D materials[97] (FIG. 2g).

2D phase transitions

A variety of 2D phase transitions have been investigated thus far. Here, we discuss notable examples, illustrating the richness of phase transformation behaviour in 2D materials.

Polymorphic phase transitions

The most prominent examples of 2D materials discovered so far that exhibit polymorphic phase transitions in near-ambient conditions are derived from chalcogenides with layered structures[10,101–106]. Compared with oxygen and most halogens (F, Cl, Br), chalcogen elements (S, Se and Te) have a relatively small electronegativity and, thus, in many chalcogenides, ionic and covalent bonding compete, which leads to the generation of structural polymorphs with different bonding configurations that are close in energy. Therefore, perturbations induced by weak external stimuli can drive polymorphic transitions in these materials. The most widely studied 2D materials exhibiting structural phase transitions are group 6 transition-metal dichalcogenide monolayers with the chemical formula MX_2, where M stands for Mo or W and X stands for S, Se or Te. Monolayer MX_2 materials have three well-known structural polymorphs[46,107], that is, 2H, 1T and 1T′ (FIG. 3a). The 2H phase has a trigonal prismatic coordination pattern, whereas the coordination patterns in the 1T and 1T′ phases are octahedral and distorted octahedral, respectively. Monolayer MX_2 in the semiconducting 2H phase has an optical bandgap in the range of 1.0–2.5 eV (REF.[108]). The 1T phase is metallic but unstable in isolation and subject to Peierls distortion[48,49]. The 1T phase spontaneously transforms into the 1T′ phase through the distortion of octahedral coordination. The 1T′ phase of monolayer MX_2 was first theoretically predicted[33] and then experimentally confirmed[34,35,109] to be a QSH insulator with a sizeable bandgap on the order of 0.1 eV (REFS[33,49,110]). The 1×2 Peierls reconstruction causes the metal-dominated *d*-band, which is typically the electron donor, to become lower in energy than the chalcogen-dominated *p*-band around the Γ-point, causing a topological band inversion and 'tying the knot' in the electronic band structure in the Brillouin zone. This gives a perfect edge conductance of $e^2/h = 1/25.813\,k\Omega$ at $T < 100$ K for 1T′-WTe_2 monolayer[35] with magnetic field dependence, and, combined with the fact that it is also a 2D superconductor at $T_c \approx 0.7$ K (REF.[111]), gives rise to the prospect of using it for topological quantum computing.

Theoretical calculations based on density functional theory (DFT) indicate that the 2H phase is the ground-state phase of all monolayer MX_2, except for WTe_2, for which the 1T′ phase has the lowest energy[48] (FIG. 3b). The energy differences between the 2H and 1T′ phases decrease in the order of $MS_2 \rightarrow MSe_2 \rightarrow MTe_2$. For MoS_2, the DFT-computed energy of the 1T′ phase is ~0.5 eV per formula unit higher than that of the 2H phase, whereas for $MoTe_2$, the DFT-computed energy is only 43 meV per formula unit higher. Thus, chemical processes are required for the transition between the 2H and 1T′ phases of MoS_2. By contrast, for $MoTe_2$, the H-to-T′ transition can be induced by non-chemical factors, including temperature[49,112], tensile strain[48,89,90], laser irradiation[50], electrostatic doping[51,113] and electric fields[52].

Chemically induced transition. The transition of MoS_2 from the 2H phase to the 1T or 1T′ phase occurs through the intercalation of alkali metals[107,114,115] by charge transfer from the *s* orbitals of alkali metals to the *d* orbitals of the transition-metal atoms. The increase in *d*-orbital filling causes the stability of the 1T or 1T′ phase to be higher than that of the 2H phase beyond

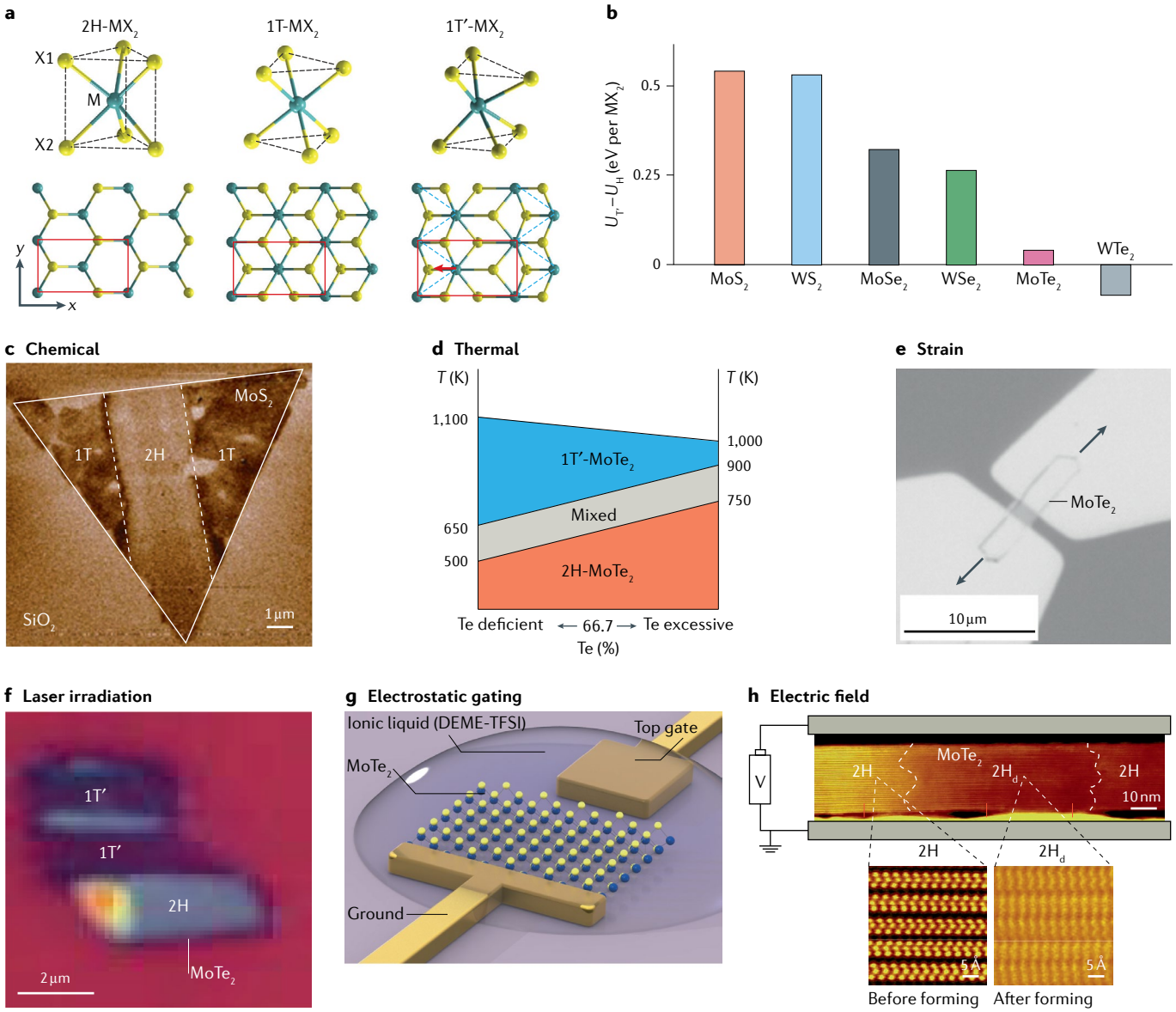

Fig. 3 | **Polymorphic transitions in 2D transition-metal dichalcogenides.** **a** | Atomistic structures of MX_2 monolayers. M represents (Mo, W) and X represents (S, Se, Te). Three structural polymorphs, that is, 2H, 1T and 1T′ phases, are shown. The red rectangles outline the unit cells. **b** | Energy differences (eV per MX_2) between the 1T′ and 2H phases ($U_{T'} - U_H$) are shown for different MX_2 monolayers, computed by density functional theory. **c** | Chemically driven polymorphic transition of MoS_2. The electrostatic force microscopy phase image shows the local conversion of a MoS_2 nanosheet from the 2H phase into the 1T phase through chemical patterning using organolithium. **d** | Thermally driven polymorphic transition of $MoTe_2$. Tellurium deficiency decreases the thermal transition temperature of $MoTe_2$ from the 2H to the 1T′ phase. **e** | Strain-driven transition of $MoTe_2$. The optical micrograph shows a $MoTe_2$ flake on a ferroelectric substrate, which can impose electric-field-induced strain on $MoTe_2$ flakes, owing to the inverse piezoelectric effect. **f** | Laser-induced patterning of $MoTe_2$ few layers from the 2H into the 1T′ phase. **g** | Schematic of an ionic liquid field-effect transistor, showing the electrostatic-doping-driven phase transition of a 2H $MoTe_2$ monolayer to the 1T′ phase. DEME-TFSI, diethylmethyl(2-methoxyethyl)ammonium bis(trifluoromethylsulfonyl) imide. **h** | Vertical-electric-field-induced formation of a conducting filament with $2H_d$ phase in 2H-$MoTe_2$. Panel **a** reprinted with permission from REF.[33], American Association for the Advancement of Science. Panel **b** reprinted with permission from REF.[112], American Chemical Society. Panel **c** adapted from REF.[47], Springer Nature Limited. Panel **d** adapted from REF.[49], Springer Nature Limited. Panel **e** adapted from REF.[90], Springer Nature Limited. Panel **f** reprinted with permission from REF.[50], American Association for the Advancement of Science. Panel **g** reprinted from REF.[51], Springer Nature Limited. Panel **h** reprinted from REF.[52,207], Springer Nature Limited.

a certain doping threshold. This phenomenon can be understood in terms of crystal field theory[10,101,116]. An incomplete doping-induced phase transition in monolayer MoS_2 can give rise to the coexistence of 2H, 1T and 1T′ phases with coherent phase boundaries[46]. The 2H phase of MoS_2 is semiconducting, whereas the 1T phase is metallic, motivating the patterning of metallic and semiconducting regions on monolayer MoS_2 by area-selective phase transformation[47] (FIG. 3c). The metallic 1T region can serve as the low-resistance contact for MoS_2 transistors, leading to improved device performance, including high drive currents, high electron mobility, low subthreshold swing values and large on/off ratios[47].

Thermally driven transition. Compared with MoS_2, the 2H and 1T′ phases of $MoTe_2$ have a smaller energy difference, enabling a wider range of external stimuli to induce the 2H-to-1T′ phase transition. Temperature alone can drive the phase transition of $MoTe_2$ from the 2H phase to the 1T′ phase, owing to the higher vibrational and electronic entropy of the 1T′ phase as compared with the 2H phase[49,112]. The transition temperature in bulk $MoTe_2$, which depends on the deficiency or excess of Te, is 500–820 °C, with Te deficiencies causing lower transition temperatures[49] (FIG. 3d). Theoretical calculations indicate that the transition temperature difference between bulk and monolayer $MoTe_2$ is modest (<20%), owing to weak phonon dispersion along the out-of-plane direction[112]. By alloying $MoTe_2$ with WTe_2, the 2H-to-1T′ phase transition temperature can be substantially decreased[112], because the 1T′ phase is the stable phase of WTe_2 at ambient conditions.

Strain-driven transition. Tensile-strain-induced transitions between the 2H and 1T′ phases of $MoTe_2$ and other MX_2 monolayers have been theoretically[48] and experimentally investigated[89,90]. The driving force for strain-induced phase transitions originates from the different unit-cell dimensions of the 2H and 1T′ phases, allowing the system to minimize the thermodynamic potential by transforming into a phase that reduces the elastic strain energy. The critical strain value needed to drive the 2H-to-1T′ phase transition is expected to depend on the mechanical boundary conditions[48]. Experimentally, a phase transition in $MoTe_2$ thin films has been demonstrated at room temperature with a 0.2% in-plane biaxial strain[89]. This level of strain can be generated by mechanical deformation of a suspended 2D material using an AFM tip[89] or through the inverse piezoelectric effect of a ferroelectric, to which the 2D material is clamped[90] (FIG. 3e).

Laser-driven transition. Laser irradiation can cause the irreversible transition of a multilayer $MoTe_2$ in the 2H phase to the 1T′ phase (FIG. 3f), owing to the generation of Te vacancies[50]. DFT calculations showed that the formation of 3% Te vacancies alters the relative stability between the 2H and 1T′ phases. This mechanism is consistent with the reduced 2H-to-1T′ thermal phase transition temperature in $MoTe_2$ with a Te deficiency[49]. Laser-induced phase transition enables the local patterning of metallic 1T′ regions in 2H-$MoTe_2$ multilayers, akin to phase patterning using chemical methods in MoS_2 (REF.[47]). The metallic 1T′ phase forms an ohmic homojunction with the semiconducting 2H phase, substantially increasing the carrier mobility of $MoTe_2$ transistors.

Electrostatic-doping-driven transition. Electrostatic doping through the application of a gate voltage can generate a carrier density of up to $10^{14}\,e\,cm^{-2}$ in monolayer MX_2 (REF.[68]), corresponding to ~0.1 e per formula unit. This feature has motivated the study of electrostatic-doping-induced structural phase transitions in MX_2 monolayers. In an electrostatic gating device configuration, in which an appropriate dielectric is sandwiched between a MX_2 monolayer and a metal plate, a gate voltage of several volts can drive a 2H-to-1T′ phase transition of monolayer $MoTe_2$, as shown by DFT-based theoretical analysis[80,113]. Electrostatic-doping-induced phase transition was further experimentally demonstrated in monolayer $MoTe_2$ using ionic liquid as the dielectric in a field-effect-transistor configuration[51] (FIG. 3g); a gate voltage of ~4 V fully converted the 2H phase into the 1T′ phase.

Electric-field-driven transition. In vertical devices based on $MoTe_2$ and $Mo_{1-x}W_xTe_2$ thin films, an electric field applied across the film thickness direction can induce the transition of MX_2 from the 2H phase into a distorted transient structure, $2H_d$, in which the monolayer structure is distinct from the three known phases of MX_2 (REF.[52]) (FIG. 3h). The exact atomic configuration of monolayers in the $2H_d$ phase has not yet been fully resolved; however, experimental evidence[52] suggests that $2H_d$ monolayers have a transitional structure, between 2H and 1T′. As a side remark, a strong enough vertical electric field can also cause topological-insulator to normal-insulator transition within the same structural polymorph[33], an extremely rapid (femtosecond level) transition in the quantum Z_2 invariant for the electronic structure.

Ferroic phase transitions

Ferroics possess two or more orientation states (domain variants), which are degenerate in free energy and can be switched by an external field[117]. Ferroics can be categorized into four types, based on the properties associated with the orientation states, that is, ferroelectrics, ferromagnets, ferroelastics and ferrotoroidics. Ferroics have been extensively studied in bulk form. Ferroelectrics show spontaneous electric polarization, which can be switched by an electric field; ferromagnets show spontaneous magnetization, which is switchable by a magnetic field; ferroelastics possess domain variants with spontaneous stress-free strain, which can be switched by applying stress; and ferrotoroidics possess internal chiral order. Ferroic materials are typically formed through ferroic phase transitions characterized by the loss of point-group symmetry operations, for example, by spatial inversion in the case of ferroelectricity, rotational symmetry in the case of ferroelasticity or time-reversal symmetry in the case of ferromagnetism[117]. A material is multiferroic if more than one ferroic order is present.

Ferroelastic transition. The high elastic strain limit and the abundance of structures with low symmetry render 2D materials promising candidates for distinct mechanical responses related to ferroelasticity. In group 6 transition-metal dichalcogenide monolayers, the 1T-to-1T′ phase transition was theoretically predicted to be a ferroelastic phase transition accompanied by spontaneous hydrostatic and shear strains[57], which has been supported experimentally[118]. The three symmetry-equivalent directions of structural distortion lead to three orientation variants with distinct unit-cell dimensions. Thus, transformation strains (also called

stress-free strains) of a variant can couple to the energetics of the system, causing the transformation from one orientation variant to another. DFT calculations suggested that a tensile strain of a few percent is sufficient to switch monolayer 1T′-WTe_2 from one orientation domain to another. Strain energy minimization can also lead to the coexistence of different domains and the stable formation of domain or phase boundaries (FIG. 4a). Monolayer 1T′-MX_2 are QSH insulators[33] and, therefore, their phase boundaries possess distinct electronic transport properties, owing to the bulk-edge correspondence in topologically non-trivial systems[119,120].

First-principles calculations have also shown that α-SnO becomes ferroelastic if the thickness of the material is at the monolayer level[121]. The low-temperature ferroelastic phase of α-SnO has an orthorhombic symmetry with two equivalent orientation states. The degenerate structural ground states can be energetically biased when illuminated with a linearly polarized laser pulse[59]. For example, when the system is subjected to an alternating electric field with a particular polarization direction, the anisotropic dielectric response of the low-symmetry ferroelastic phase will lead to a non-degenerate free energy landscape along the reaction coordinate of the phase transformation, which is similar to optical tweezing of dielectric microbeads, but along the generalized reaction coordinate of the phase transformation instead of the *x*–*y* position of a bead. Phase-change materials

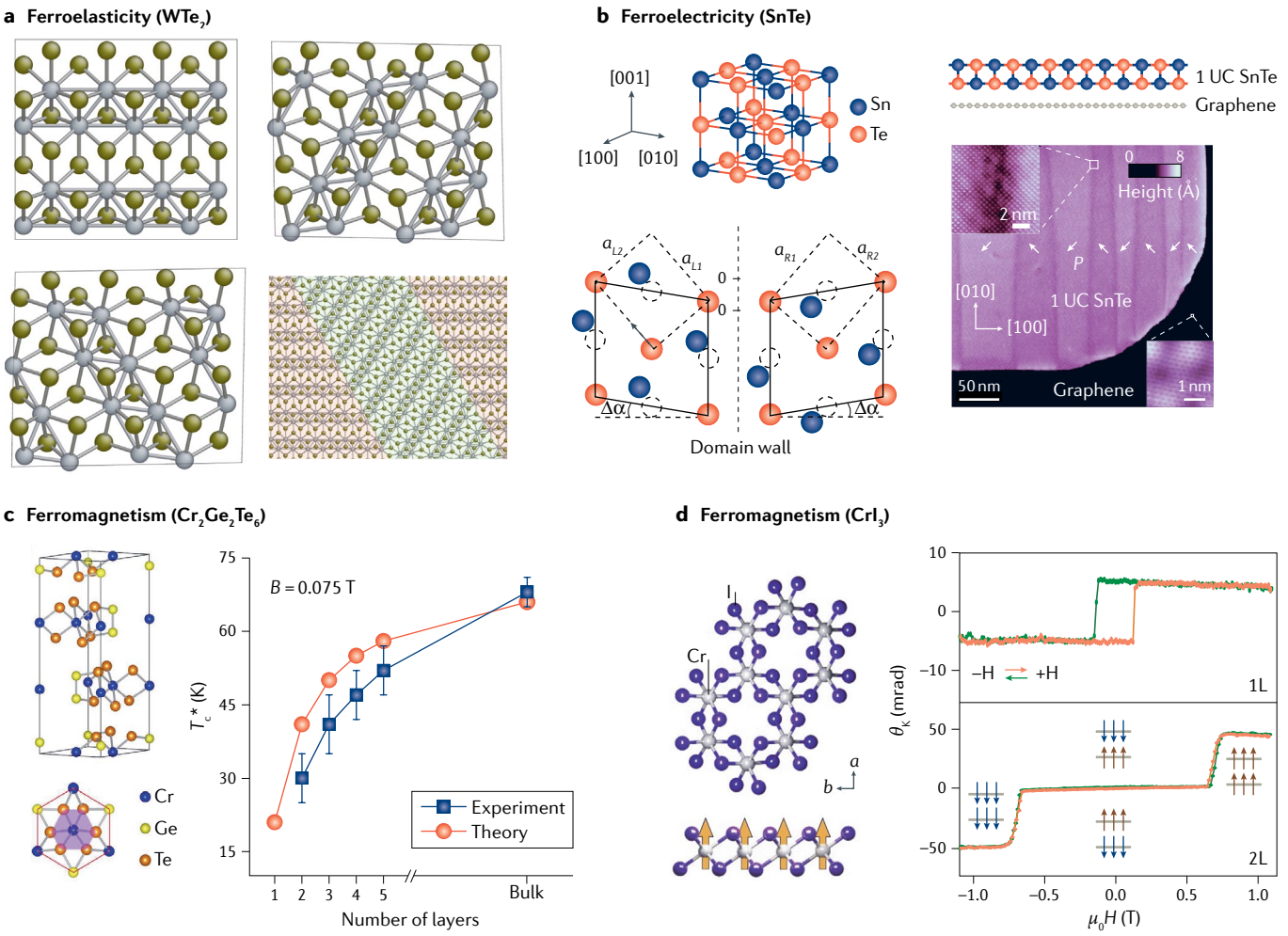

Fig. 4 | **Ferroic phase transitions in 2D materials. a** | Symmetry-equivalent orientation states and ferroelasticity in monolayer 1T′-WTe_2. The three orientation variants have slightly different spontaneous strains with respect to the parental 1T phase, which allows strain-induced switching from one orientation to another. The atomistic model shows domain boundaries formed between two orientation variants. **b** | Ferroelectricity in atomically thin SnTe. Schematic of the crystal structure of SnTe and SnTe thin films is shown with a thickness of one unit cell (UC). Lattice distortion and atomic displacements are illustrated in the ferroelectric phase. Two symmetry-equivalent distortion directions lead to two variants of ferroelectric domains separated by domain walls, as shown in the scanning tunnelling microscope image of atomically thin SnTe, coloured in purple. **c** | Ferromagnetism in $Cr_2Ge_2Te_6$ atomic layers. The crystal structure of $Cr_2Ge_2Te_6$ and the layer-dependent ferromagnetic transition temperature under a perpendicular magnetic field of 0.075 T are shown, obtained from experimental measurements (blue squares) and theoretical calculations (orange spheres). **d** | Ferromagnetism in atomically thin CrI_3. The crystal structure of a monolayer CrI_3 and the Kerr rotation angles (θ_k) of monolayer (1L) and bilayer (2L) CrI_3 as a function of the perpendicular magnetic field ($\mu_0 H$) are shown, providing evidence of magnetic ordering. Insets schematically show the magnetic ground states of the systems under different field strengths. Panel **a** reprinted from REF.[57], CC BY 4.0 (https://creativecommons.org/licenses/by/4.0/). Panel **b** reprinted with permission from REF.[55], American Association for the Advancement of Science. Panel **c** reprinted from REF.[40], Springer Nature Limited. Panel **d** adapted from REF.[39], Springer Nature Limited.

have been proposed to operate on the basis of such optomechanically driven 2D martensitic transitions[59,60], which have multiple advantages compared with traditional, thermally driven phase-change systems (such as Ge-Sb-Te alloys), including faster transformation kinetics, reduced energy dissipation and more robust resistance against functional fatigue.

Ferroelectric transition. Ferroelectricity in thin-film perovskite materials has been intensively studied[122]; however, in ferroelectrics with out-of-plane polarization, the ferroelectric order disappears if the film thickness is below a critical value, owing to the effects of the depolarization field and surface reconstruction[122,123]. By contrast, in-plane polarization is less susceptible to the thickness-dependent depolarization effect, and, thus, ferroelectric order may remain stable in 2D. Indeed, robust in-plane ferroelectricity has been experimentally realized in atomic-thick SnTe, with a ferroelectric transition temperature of 270 K (REF.[55]) (FIG. 4b). Ferroic phase transitions have also been theoretically investigated in group IV monochalcogenide MX (M = Ge, Sn; X = S, Se), which are closely related to SnTe (REFS[58,124–128]). MX monolayers can further be ferroelectric and ferroelastic at the same time, making them multiferroic[58,124].

Ferroelectricity has also been experimentally demonstrated in other 2D systems, including In_2Se_3 (REFS[56,129–132]), $CuInP_2S_6$ (REFS[133,134]), monolayer $MoTe_2$ with distorted 1T phase[135,136], as well as bilayers and trilayers of WTe_2 (REF.[70]). Notably, 2D α-In_2Se_3 possesses both out-of-plane and in-plane ferroelectric orders, and the out-of-plane polarization is resistant to the depolarization field owing to the locking between out-of-plane dipoles and in-plane lattice asymmetry[56,131]. Furthermore, out-of-plane ferroelectricity can be present in 2D semimetals, for example, in few-layer WTe_2, because dielectric screening in the layer-normal direction is suppressed in a 2D system. Remarkably, ultrafast symmetry switching behaviour was observed in 3D bulk WTe_2 (REF.[53]), a type II Weyl semimetal[137]. In contrast with monolayer 1T′-WTe_2, which is centrosymmetric, multilayer and bulk WTe_2 have an orthorhombic structure with distorted octahedral coordination and broken inversion symmetry (the T_d phase, space group $Pmn2_1$)[138]. Upon electric gating along the layer-normal direction, multilayer WTe_2 shows ferroelectric switching with a butterfly-shaped conductance curve[54,70]. Different from local atomic-movement-induced ferroelectric transition[139] (for example, through breaking and switching of local W–W bonds or by local distortion and rotation of W–Te bonds), low-energy interlayer gliding is likely responsible for the switching behaviour in multilayer and bulk WTe_2 (REFS[71,140]).

Ferromagnetic transition. A consequence of the Hohenberg–Mermin–Wagner theorem[12,13] is that long-range ferromagnetism cannot exist at finite temperature in 2D, if the spin Hamiltonian has a continuous symmetry with sufficient short-range interactions[13], as ample gapless spin waves will destroy the ferromagnetic state. However, ferromagnetism can be stabilized at finite temperature if magnetic anisotropy is present in the system[141–143]. Furthermore, finite size effects can stabilize phase transitions in 2D, including a ferromagnetic transition, because the divergence of fluctuations in 2D is only logarithmic with sample size and, thus, a slow divergence[62]. Ferromagnetism has been experimentally observed in a range of 2D materials[41–45], including semiconducting $Cr_2Ge_2Te_6$ (REF.[40]), CrI_3 (REF.[39]), CrXBr (X = S, Se)[144–147] and metallic Fe_3GeTe_2 (REFS[70,148,149]) (FIG. 4c,d).

High-temperature diffusive phase changes

In diffusive transformations, changes in labelled atomic registries are non-deterministic, and the macroscopic order parameters of the new phase or domain do not reveal detailed atom-to-atom correspondences between the old and new phases, because changes in the registry are caused by multiple randomized atomic hops. By contrast, in an ideal displacive transformation, the nearest-neighbour relation of an atom either remains unchanged or changes in a deterministic way within a domain variant. Displacive transformations are often driven by a strong directional field, for example, stress, an electric field or a magnetic field. Most ferroelastic and ferroelectric transitions, which involve the loss of rotational symmetry or spatial inversion symmetry, are displacive transformations. The kinetics of displacive transformations are characterized by a threshold-type behaviour of the domain-growth speed v with respect to the thermodynamic driving force F; the nonlinear $v(F)$ is nearly zero below a certain threshold, but substantially increases above a threshold F_{thresh}, and then saturates at the phonon group velocity. The growth speed of a displacive phase-change domain thus has to be fitted by a highly nonlinear function $v \propto (F/F_{thresh})^n$, where n can be as large as 20. In comparison, diffusive transformations have a more linear-response-type growth velocity law $v(F)$, where n is 1 or close to 1, but is often much more temperature-sensitive.

Diffusive motion is usually thermally activated and, therefore, more prevalent at high temperatures, at which atomic defects have higher concentration and also become more labile, allowing the system to fully sample the configurational space (entropy), which results in an optimal organization (phase) and, thus, approaching the equilibrium phase diagram. By changing the chemical precursors during chemical vapour deposition, 2D [Mo,W]S_2 forms either a two-phase MoS_2/WS_2 heterostructure with sharp phase boundaries at 650 °C or a single-phase random solid-solution $Mo_xW_{1-x}S_2$ at ≥680 °C (REF.[150]) (FIG. 5a). Compared with lattice diffusion in 3D crystals, diffusion in 2D crystals is easier because surface diffusivity is commonly acknowledged to be much faster than bulk diffusivity. The phase-separated MoS_2/WS_2 heterostructure can be applied in optoelectronics and the solid-solution $Mo_xW_{1-x}S_2$ alloy phase can be used to tune the relative phase stabilities of different polymorphs (2H, 1T and 1T′) by changing the Mo/W ratio. Generally speaking, at high temperatures, it is important to probe and precisely navigate the equilibrium temperature-composition phase diagram.

The size, morphology and defect content of 2D materials not only depend on the composition but also on the growth conditions (FIG. 5b). For example, large-area

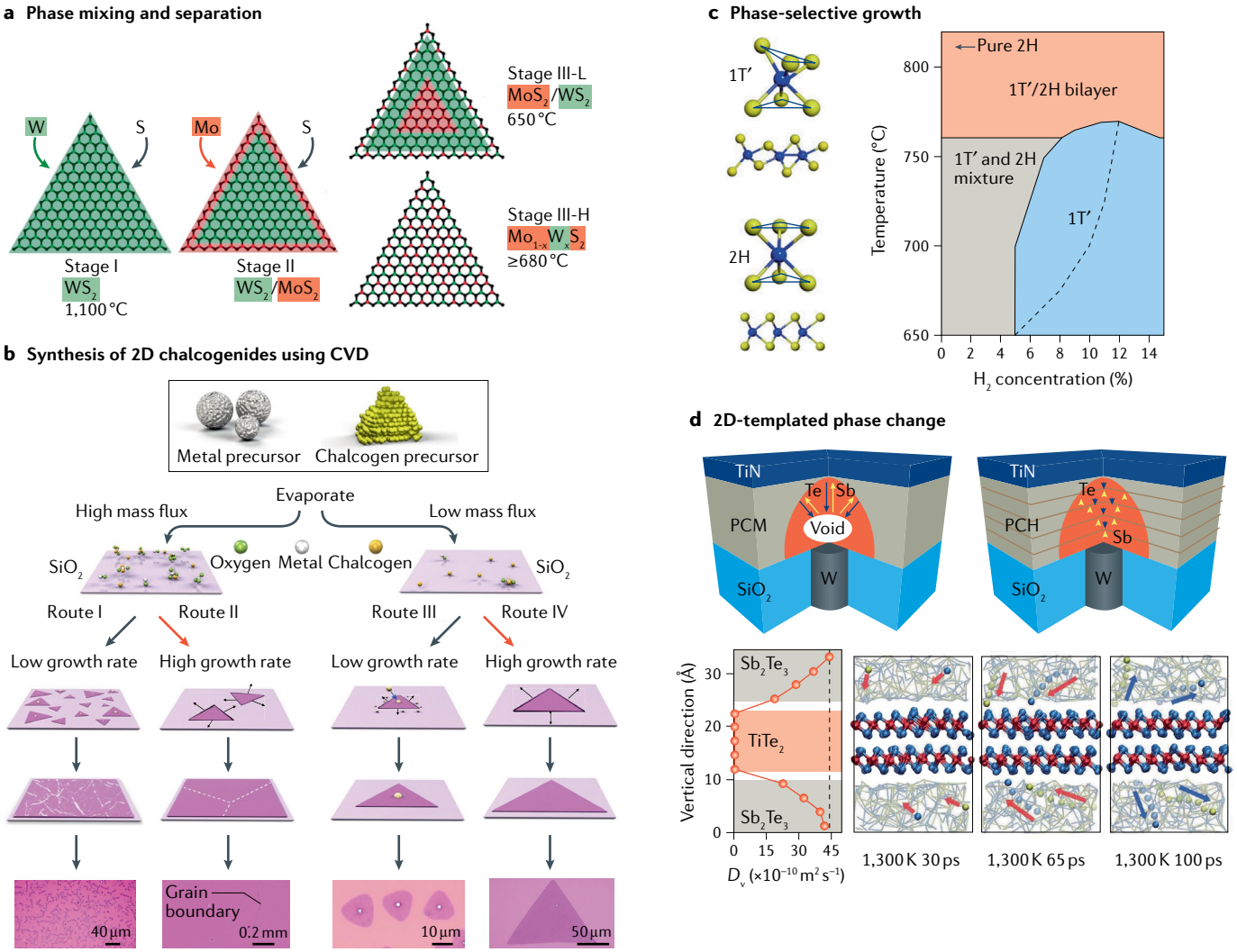

Fig. 5 | **2D or 2D-templated diffusive phase transitions. a** | Chemical vapour deposition (CVD) growth of a phase-separated MoS_2/WS_2 heterostructure and solid-solution $Mo_xW_{1-x}S_2$ alloy. Compositional mixing and segregation are favoured at high and low growth temperatures, respectively. **b** | Synthesis of 2D transition-metal chalcogenides by CVD. The morphology and defect content of 2D transition-metal chalcogenides depend on the growth kinetics, including mass flux of metal precursors and growth rate. **c** | Phase diagram for the growth of the 1T′ and 2H phases of a MoS_2 monolayer using K_2MoS_4 as the growth precursor. Controlled growth of 1T′ and 2H phases can be realized by varying the growth temperature and H_2 concentration. **d** | 2D-templated diffusive phase transition in a $TiTe_2/Sb_2Te_3$ phase-change heterostructure (PCH). The 2D $TiTe_2$ layers, which have a lower diffusion coefficient (D_v) than the Sb_2Te_3 layers, block the electrical-field-assisted transport of charged species in the Sb_2Te_3 diffusive switching layers, leading to less noise and drift for memory operation than traditional phase-change memory (PCM) materials. Panel **a** adapted with permission from REF.[150], American Chemical Society. Panel **b** adapted from REF.[151], Springer Nature Limited. Panel **c** reprinted from REF.[155], Springer Nature Limited. Panel **d** reprinted with permission from REF.[159], American Association for the Advancement of Science.

growth of 2D metal chalcogenides can be achieved by using molten salt as a growth medium[151], which reduces the melting point of metal-ion-bearing precursors and allows passivation of different growth edges[152]. Moreover, under out-of-thermal-equilibrium conditions, for example, under external irradiation (photons, electrons), electrical current or plasma treatment, phase changes can occur in a manner that does not abide by the equilibrium phase diagram[153]. In addition, conditions can be designed to directly grow thermodynamically metastable phases[105,154,155] (FIG. 5c).

2D and 2D-templated diffusive phase transformations have played a key role in the development of phase-change memory (PCM) materials. PCM provided the basis for information storage in CDs and DVDs, as well as for the newest generation of non-volatile solid-state drives. For example, sub-nanosecond writing has been achieved with $Sc_{0.2}Sb_2Te_3$ as the active crystalline-to-amorphous phase-change material[156]. However, several challenges remain to be addressed, including high-temperature-induced volatility and resistance-level drifting[157], which will require a thorough understanding and fine control of the ionic motion during device operation. Owing to their atomic thickness, 2D active materials have distinct thermal conduction characteristics and phase transformation kinetics, featuring less elastic energy constraints, facile diffusion kinetics and sensitive coupling to external conditions, as

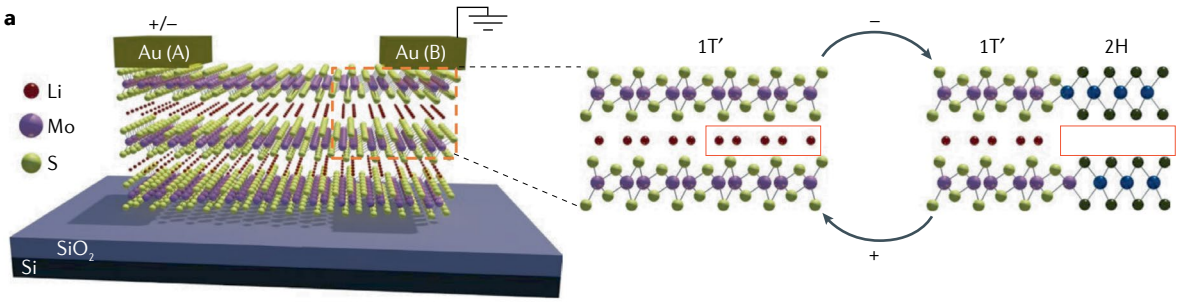

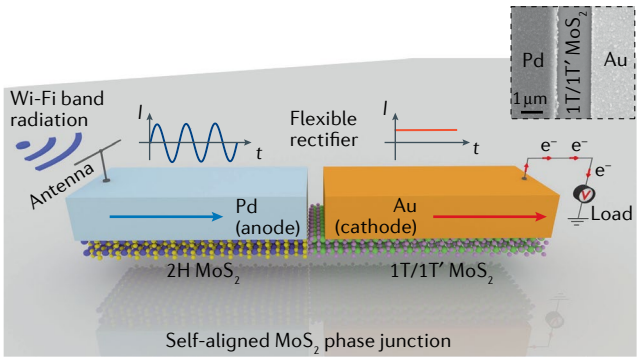

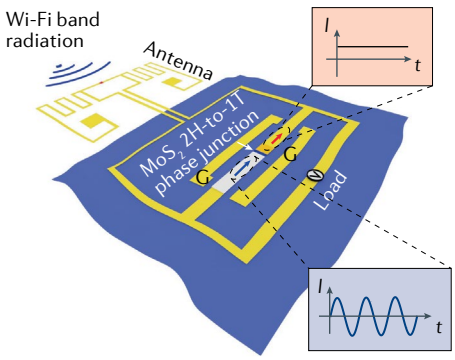

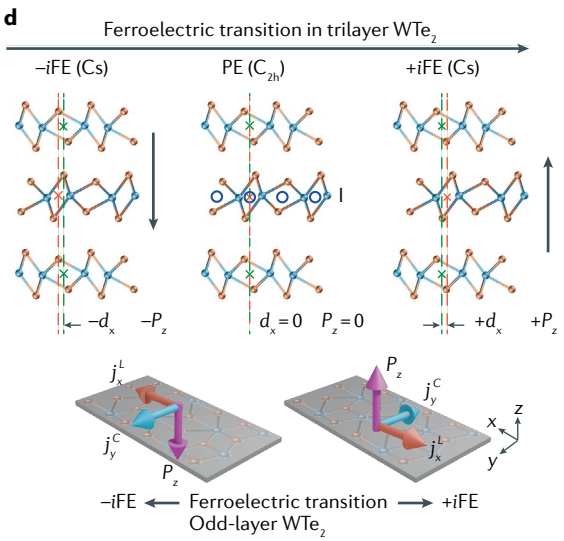

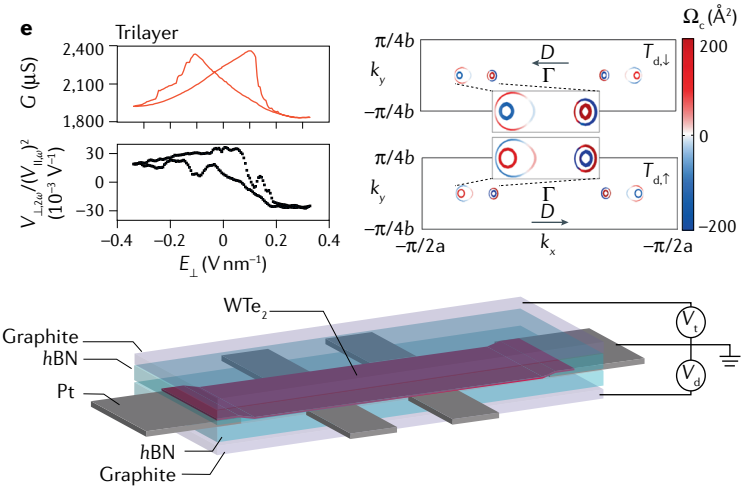

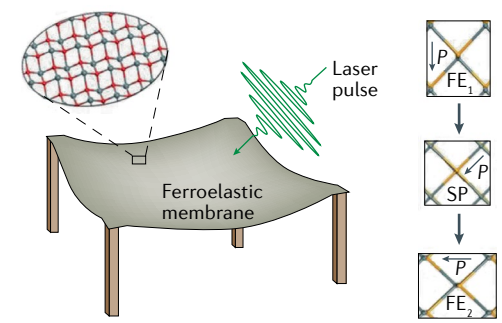

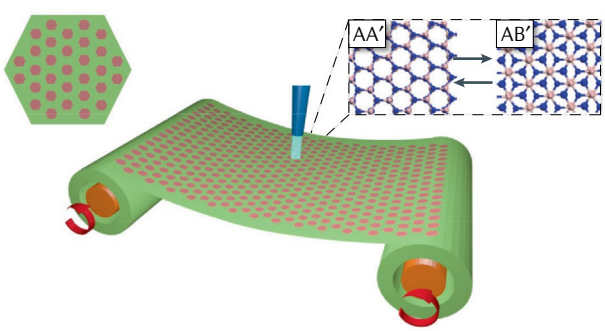

compared with 3D bulk materials. These characteristics can be exploited to improve the temperature-driven read, write and storage performance of PCM devices, increasing speed, reducing energy consumption and increasing storage density. For example, in a PCM device constructed from a 2D Sb_2Te_3-GeTe superlattice, the diffusion of Ge and Te atoms within 5-Å-thick GeTe 2D crystal layers can be modulated by the immobile and strained Sb_2Te_3 2D crystal layer[158]. The strained Sb_2Te_3 layer affects the quenching-to-amorphous and crystallization kinetics of the GeTe layer in the van der Waals heterostructure, leading to increased atomic diffusivity in the

Fig. 6 | **New device applications of 2D phase-change materials. a** | Schematic of the reversible 2H-to-1T′ phase transition of Li_xMoS_2 films through electric-field-controlled migration of Li^+ ions. An increase in Li^+ ion concentration causes the transformation of the 2H phase into the 1T′ phase, and vice versa. Such reversible local phase transitions impart electronic devices with excellent memristive properties[162]. **b** | Schematic of a MoS_2 lateral Schottky diode, with the core component including a MoS_2 semiconducting-metallic (2H-to-1T/1T′) phase junction. The resulting low resistance and ultralow junction capacitance allow fabrication of a flexible and ultrafast rectifier that can generate D.C. electricity from A.C. signals at a frequency up to 10 GHz. **c** | Combining the high-speed rectifier with a flexible antenna results in a flexible rectenna that can harvest wireless radio-frequency energy at the Wi-Fi-band. **d** | The ferroelectric nonlinear anomalous Hall effect in time-reversal invariant systems provides the theoretical basis for nonlinear memory. Nonlinear anomalous Hall current switches in odd-layer WTe_2 but remains invariant in even-layer WTe_2 upon ferroelectric transition. P_z is the electric polarization along the z direction and d_x indicates the offset of the inversion centres between the middle and top/bottom layers along the x direction. Two ferroelectric states are related to each other by an inversion operator, denoted as $+i$FE and $-i$FE, respectively. Upon the ferroelectric transition, a nonlinear anomalous Hall current j_x^L switches between the $-x$ and $+x$ directions under an external field with in-plane linear polarization, owing to the linear photogalvanic effect, while a nonlinear anomalous Hall current j_y^C switches between the $-y$ and $+y$ directions under circularly polarized light with normal incidence, owing to the circular photogalvanic effect. **e** | Experimental demonstration of the ferroelectric nonlinear anomalous Hall effect and Berry curvature memory in trilayer WTe_2. Nonlinear Hall voltage can be easily detected, and its sign informs the memory state directly. $V_{\perp,2\omega}$ and $V_{\parallel,\omega}$ are the nonlinear transverse voltage at frequency 2ω and nonlinear longitudinal voltage at frequency ω, respectively. The ratio of $V_{\perp,2\omega} / (V_{\parallel,\omega})^2$ is proportional to the Berry curvature dipole D. As the electric field $E_\perp$ switches, the longitudinal conductance G shows a butterfly-shape hysteresis, while $V_{\perp,2\omega} / (V_{\parallel,\omega})^2$ switches the sign, indicating the flipping of Berry curvature dipole D. This is reflected in the Berry curvature Ω_c distribution in the two-dimensional k_x–k_y Brillouin zone. **f** | Optomechanical martensitic transition induced by a linearly polarized laser pulse in ferroelastic monolayer SnO (left) and SnSe (right). SnSe is multiferroic, showing both ferroelastic and ferroelectric order. Displacive domain switching associated with the optomechanical martensitic transition is accompanied by the switching of polarization directions (FE_1 and FE_2). SP is the saddle point of ferroelastic and ferroelectric switching. **g** | Scrollable optical disk drive based on the optomechanically driven transition in bilayer hexagonal boron nitride. Upon illumination by a laser pulse, the layer stacking pattern of each bilayer hexagonal boron nitride domain can switch from AA′ to AB′. The size of each domain is comparable to the spot size of the laser. The optical disk drive contains a lattice of domains, which can be scrolled to increase data density. Panel **a** adapted from REF.[162], Springer Nature Limited. Panels **b** and **c** adapted from REF.[163], Springer Nature Limited. Panel **d** adapted from REF.[140], CC BY 4.0 (https://creativecommons.org/licenses/by/4.0/). Panel **e** adapted from REF.[54], Springer Nature Limited. Panel **f** adapted with permission from REF.[59], American Chemical Society. Panel **g** reprinted from REF.[60], Springer Nature Limited.

active layer and higher energy efficiency of the device. Similarly, 2D $TiTe_2$/3D Sb_2Te_3 phase-change heterostructures also show ultralow noise and drift[159]. The 2D $TiTe_2$ layers in the heterostructure suppress damage in the 3D Sb_2Te_3 structure by blocking the electrical-field-assisted transport of charged species (FIG. 5d).

Technological applications

The possibility to change material properties by 2D phase transitions, which can be coupled to external stimuli, enables a broad range of potential device applications. For example, the 2H-to-1T or 2H-to-1T′ phase change of transition-metal dichalcogenides can be induced by alkali metal intercalation, which can be exploited to improve the electrocatalytical performance of these materials for electrochemical hydrogen gas evolution[100] or to fabricate lateral heterostructures of semiconducting and metallic phases for 2D electronic devices with low contact resistance[47,101]. Such ohmic lateral heterophase junctions formed between the semiconducting 2H and metallic 1T′ phases of $MoTe_2$ can also be fabricated by laser-induced phase transition, which causes the 2H-to-1T′ transition of $MoTe_2$ as a result of the creation of Te vacancies[50].

The electrical and/or optical property changes associated with 2D phase transitions are particularly interesting for the fabrication of non-volatile memories and transport devices. For example, resistive random access memories and ferroelectric phase-change transistors have been designed based on electric-field-induced[52] and strain-induced[90] 2H-to-1T′ phase transitions of transition-metal dichalcogenides, respectively. Since the 1T′ phase of group 6 monolayer transition-metal dichalcogenides is a QSH insulator[33], controlling their topological electronic properties based on the above phase transition can potentially enable the design of new quantum electronic devices.

2D materials with ferroic phase transitions and properties enable the design of a range of ultrathin and flexible smart materials and functional devices, with potential usages in micro/nano systems and conformal devices; for example, 2D ferroelastics can be used for nanoscale actuators and shape-memory materials[57]; 2D ferroelectrics can be applied for memory devices[55] and ferroelectric tunnel junctions[160]; and 2D ferromagnets can be used for spintronics[42,44]. Certain 2D multiferroics, such as group IV monochalcogenides, can exhibit strong coupling between ferroelectric and ferroelastic orders, as well as strong and anisotropic excitonic absorption[161], making them attractive for the development of 2D ferroelectric memory, 2D ferroelastic memory, 2D nonvolatile photonic memory and 2D ferroelectric excitonic photovoltaics[58].

Several novel device prototypes that take advantage of phase transitions in 2D materials have been experimentally demonstrated. For example, excellent memristive behaviour can be achieved by exploiting the reversible 2H-to-1T′ phase transition of layered MoS_2 films, driven by electric-field-induced Li^+ ion redistribution, for example, for the implementation of artificial neural networks in neuromorphic computing[162] (FIG. 6a). Metallic-semiconducting (1T/1T′-to-2H) phase heterojunctions of MoS_2 layers have been used to fabricate atomically thin and flexible lateral Schottky diodes with ultralow junction capacitance and low series resistance. These Schottky diodes enable the design of flexible and ultrafast rectifiers, which can convert A.C. electrical signals' waves into D.C. electricity at a frequency of up to 10 GHz. Such flexible rectennas can harvest wireless radio-frequency energy at the Wi-Fi band[163] (FIG. 6b,c).

In addition, ferroelectricity-driven nonlinear photocurrent switching and a ferroelectric nonlinear anomalous Hall effect have been theoretically predicted[140,164] and experimentally demonstrated[54] in time-reversal invariant few-layer WTe_2. Upon ferroelectric transition in few-layer WTe_2, nonlinear anomalous Hall voltage switches the sign in odd-layer WTe_2 (except monolayer 1T′-WTe_2) but remains invariant in even-layer WTe_2 (FIG. 6d,e). This oscillation originates from the absence and presence of Berry curvature dipole reversal and shift dipole reversal, owing to distinct ferroelectric transformations in even-layered and odd-layered WTe_2 (REF.[140]).

These theoretical predictions and experimental demonstrations establish Berry curvature and shift dipole as nonlinear order parameters, opening a route towards unconventional memory devices, such as a Berry curvature memory based on nonlinear susceptibility. Weak interlayer gliding in WTe_2 also offers a strategy to engineering and controlling 2D ferroelectric patterns by electric gating and optical switching, enabling high speed and low activation energy for electromechanical, optomechanical and neuromorphic applications.

Finally, optomechanical devices could benefit from the strong coupling between 2D phase-change materials and light, as well as from the extraordinary mechanical properties of 2D materials. For example, a linearly polarized laser pulse can drive an ultrafast diffusionless martensitic phase transition of 2D ferroelastic materials, for example, of monolayer SnO and SnSe (REF.[59]). Memory devices based on such optomechanical martensitic transitions require an order of magnitude lower energy input than traditional Ge-Sb-Te alloys[59] (FIG. 6f). In bilayer hexagonal boron nitride, a laser with selected frequency can modify the energetics of different (meta-) stable stacking patterns, and reversibly and controllably switch the stacking patterns without barriers, making this material attractive for data storage and optical phase masks[60] (FIG. 6g).

Outlook

To enable the industrial applications of 2D materials, the realization of large-area growth of high-quality materials, facile and robust material processing, high-performance devices and systems, as well as long service lifetimes, all need to be achieved. The phase behaviour of 2D materials is important in all these growth-processing-service steps. Furthermore, phase transitions have long been explored to improve or enable distinct material functionalities. In particular, 2D phase transitions have a variety of unique features, which can be exploited for electronic, optical, magnetic, electromechanical[165], optomechanical[59] and magnetomechanical[166] systems. However, important challenges remain to be addressed in the field of 2D phase transitions.

Discovery and characterization of new 2D phase-change materials

Most known 2D phase-change materials are derived from chalcogenides that have a layered bulk structure. Expanding the portfolio of 2D phase-change materials will open new application spaces. In principle, 2D phase-change materials could exist in a range of materials systems, either in a free-standing or in a substrate-supported form, for example, oxides, pnictides and halides. First-principles calculations can play a key role in the discovery of new phase-change materials; for example, crystal structure prediction tools[167] and machine learning[168–170] could be applied to explore the free energy landscape and discover new 2D phase-change materials, which may not even have a bulk counterpart. Importantly, certain phase-change 2D materials could be entropically stabilized at high temperatures, as a result of large configurational entropy (compositional complexity)[171] or vibrational entropy (owing to the presence of soft phonon modes or strong lattice anharmonicity)[172], and remain stable or metastable at room temperature. These materials may not be accessible in traditional structural prediction algorithms[167] or from the mining of existing crystallographic databases[173–177], because, at present, these approaches typically do not consider the entropy contribution to phase stabilization.

Understanding the kinetics and controlling 2D phase transitions

The thermodynamics of 2D phase transitions have been extensively studied; however, the kinetics of 2D phase transitions remain less explored. In 2D materials, the transformation interfaces and pathways are expected to be substantially different than in bulk materials. Understanding the kinetics is required to precisely control 2D phase transitions. In situ structural studies during phase transitions may be performed in real space (for example, by in situ TEM[178]) or in reciprocal space (for example, by in situ X-ray diffraction[179] or ultrafast electron diffraction[180]). In parallel with structural evolution, the accompanying changes in electronic structure, vibrational spectra or symmetry properties can be probed by time-resolved angle-resolved photoemission spectroscopy (tr-ARPES)[181], time-resolved infrared and Raman spectroscopy or time-resolved second-harmonic generation (SHG) spectroscopy[182], respectively. Recent advances in ultrafast dark-field electron microscopy further allow the real-space imaging of order-parameter dynamics during structural phase transitions in transition-metal dichalcogenides with nanometre spatial and femtosecond temporal resolution[183]. Combining in situ TEM experiments, aberration-corrected TEM imaging of atomic-level structural evolution[76], and dark-field TEM imaging of order-parameter and microstructural dynamics[183,184], allows a multiscale view of the kinetics of 2D structural phase transitions driven by a variety of stimuli.

Flexural engineering of 2D phase transitions

The flexural mode[73,185] in 2D materials offers the possibility to control and configure 2D phase transitions, which is difficult to achieve in bulk materials; for example, giant pseudomagnetic fields[98] and exciton funnelling[99] in inhomogeneously strained 2D materials. Flexoelectric, flexomagnetic and flexooptic couplings likely affect 2D phase transitions, which may allow precise control of phase changes at a desired temperature and spatial location, by configuring specific structural patterns (for example, ripples). Such periodic patterns could be achieved by stacking 2D materials on a soft substrate, followed by mechanical deformation (for example, tension and compression) or temperature change (for example, by using substrates with different thermal expansion coefficient), to construct periodically patterned ripples and wrinkles. Here, the combination of out-of-plane interfacial energy and in-plane patterns may affect the phase transition. In addition, in 2D materials stacked on a substrate with a large lattice mismatch or finite twisting angle, spatial inhomogeneity in the interlayer interaction and separation is naturally induced, which leads to the creation of tunable periodic structures with a strain gradient and flexoelectricity, as

observed in Moiré superlattices[186]. The flexoelectricity could be exploited to control local deformation and, thus, phase transitions by external electric field.

Phase transitions in stacked 2D materials and van der Waals heterostructures

Monolayer 2D materials have ultrathin thickness and cover a wide variety of electronic structural types (metals, semiconductors, insulators, topological insulators and topological metals[33]). The absence of surface dangling bonds and the weak van der Waals interactions between layers enable the construction of stacked layers and van der Waals heterostructures with infinite possibilities[93]. In such stacked materials, there is a hierarchy in the bonding energy scales between intralayer and interlayer interactions (covalent versus mostly van der Waals, with the former being much stronger[71,187]) in stacked layers, yet, the interlayer electronic interactions can still be strong and have a considerable influence on the properties of the resulting materials. The emergence of flat bands and strong-correlation physics in stacked bilayer graphene with a twisting angle, including superconductivity transitions[27,30,188,189], as well as the transition of monolayer MoS_2 from a direct-bandgap semiconductor to an indirect-bandgap semiconductor in bilayers[64], are eminent examples.

Phase transitions of 2D materials become richer in stacked 2D materials and van der Waals heterostructures, as, in addition to monolayer structural degrees of freedoms (polymorphs, domain variants and ripples), additional stacking degrees of freedom (stacking materials and stacking order, including the relative shifts and orientation angles between layers[190]) also come into play. These stacking degrees of freedom are often easier to manipulate, because the energy barriers between stacking orders are usually smaller than the monolayer structural degrees of freedom, owing to weak interlayer bonding interaction, thus, facilitating their control by external stimuli. The interplay between multiple external fields (electrical, optical, magnetic, thermal, mechanical or chemical), monolayer phase transitions and stacking phase transitions can result in rich materials responses by altering band structures and topologies[53], electron–phonon interactions and electron–electron correlations[27,30], to name a few, leading to new fundamental discoveries and device concepts. As an example of a phase transition driven by a change in layer stacking geometry, electrically driven interlayer sliding in few-layer WTe_2 accompanied by ferroelectricity and the ferroelectric nonlinear anomalous Hall effect based on Berry curvature dipoles open up avenues for the development of 2D semimetal-based memory devices[54]. This concept can be expanded to ferroelectric few-layer 2D semiconductors (for example, monolayer GeSe and SnTe)[164] and topological quantum materials (for example, $MnBi_2Te_4$, which shows a quantum anomalous Hall effect)[191]. For example, a ferroelectric transition could be induced in odd-layer GeSe or SnTe, and the corresponding shift current response could be measured. Demonstration of shift current switching would provide the experimental foundation for realizing shift-dipole-based nonlinear memory[164]. Furthermore, optomechanics could play a key role in the phase engineering of stacked 2D materials by shifting interlayer stacking configurations through altering the energy landscape by a light field with a selected frequency[60] or through the excitement of coherent phonons by terahertz light[192], driving the system into a metastable or more stable phase. This kind of strongly nonlinear light–matter interactions, driving phonon–polaritons to the nonlinear regime and even beyond the convex part of the phonon energy landscape, could lead to a variety of nonlinear optical and stimulated emission effects that are quantum mechanical in nature. Optomechanics could also result in the change of the twist angles of stacked 2D materials, either through the direct change of orientation degrees of freedom accompanying a light-induced ferroelastic transition[59] or by the mechanical coupling to the strain induced by optomechanical phase transitions, thus, contributing a useful set of tools in the emerging field of twistronics[189,193–195].

The rapid progress in semiconductor technology has given us Moore's law. Commercial transistors can now be produced with a feature size of 5 nm, which may soon be reduced to 3 nm and below[196]. Applying 2D materials exhibiting phase transitions could address the challenge of further miniaturization, resulting in more energy-efficient and faster memory[54,80], computing[33], sensing and actuating[57,59] devices. Therefore, research in this area will not only produce fundamental new knowledge but will also play a crucial role in the development of new devices and technologies in the coming decades.

Published online 9 April 2021

1. Ma, S. *Modern Theory of Critical Phenomena* (W. A. Benjamin, Advanced Book Program, 1976).
2. Goldenfeld, N. *Lectures on Phase Transitions and the Renormalization Group* (Addison-Wesley, 1992).
3. Christian, J. W. *The Theory of Transformations in Metals and Alloys* 3rd edn (Pergamon, 2002).
4. Sachdev, S. *Quantum Phase Transitions* 2nd edn (Cambridge Univ. Press, 2011).
5. Fradkin, E. *Field Theories of Condensed Matter Physics* 2nd edn (Cambridge Univ. Press, 2013).
6. Novoselov, K. S. et al. Two-dimensional atomic crystals. *Proc. Natl Acad. Sci. USA* **102**, 10451–10453 (2005).
7. Wang, Q. H., Kalantar-Zadeh, K., Kis, A., Coleman, J. N. & Strano, M. S. Electronics and optoelectronics of two-dimensional transition metal dichalcogenides. *Nat. Nanotechnol.* **7**, 699–712 (2012).
8. Novoselov, K. S., Mishchenko, A., Carvalho, A. & Castro Neto, A. H. 2D materials and van der Waals heterostructures. *Science* **353**, aac9439 (2016).
9. Manzeli, S., Ovchinnikov, D., Pasquier, D., Yazyev, O. V. & Kis, A. 2D transition metal dichalcogenides. *Nat. Rev. Mater.* **2**, 17033 (2017).
10. Yang, H., Kim, S. W., Chhowalla, M. & Lee, Y. H. Structural and quantum-state phase transitions in van der Waals layered materials. *Nat. Phys.* **13**, 931–937 (2017).
11. Onsager, L. Crystal statistics. I. A two-dimensional model with an order-disorder transition. *Phys. Rev.* **65**, 117–149 (1944).
12. Hohenberg, P. C. Existence of long-range order in one and two dimensions. *Phys. Rev.* **158**, 383–386 (1967).
13. Mermin, N. D. & Wagner, H. Absence of ferromagnetism or antiferromagnetism in one- or two-dimensional isotropic heisenberg models. *Phys. Rev. Lett.* **17**, 1133–1136 (1966).
14. Kosterlitz, J. M. & Thouless, D. J. Long range order and metastability in two dimensional solids and superfluids. (Application of dislocation theory). *J. Phys. C Solid State Phys.* **5**, L124–L126 (1972).
15. Kosterlitz, J. M. & Thouless, D. J. Ordering, metastability and phase transitions in two-dimensional systems. *J. Phys. C Solid State Phys.* **6**, 1181–1203 (1973).
16. Klitzing, K. V., Dorda, G. & Pepper, M. New method for high-accuracy determination of the fine-structure constant based on quantized hall resistance. *Phys. Rev. Lett.* **45**, 494–497 (1980).
17. Tsui, D. C., Stormer, H. L. & Gossard, A. C. Two-dimensional magnetotransport in the extreme quantum limit. *Phys. Rev. Lett.* **48**, 1559–1562 (1982).
18. Binnig, G., Rohrer, H., Gerber, C. & Weibel, E. Surface studies by scanning tunneling microscopy. *Phys. Rev. Lett.* **49**, 57–61 (1982).

19. Binnig, G., Quate, C. F. & Gerber, C. Atomic force microscope. *Phys. Rev. Lett.* **56**, 930–933 (1986).
20. Binnig, G., Rohrer, H., Gerber, C. & Weibel, E. 7 × 7 reconstruction on Si(111) resolved in real space. *Phys. Rev. Lett.* **50**, 120–123 (1983).
21. Zhang, J., Liu, J., Huang, J. L., Kim, P. & Lieber, C. M. Creation of nanocrystals through a solid-solid phase transition induced by an STM tip. *Science* **274**, 757–760 (1996).
22. Kaganer, V. M., Möhwald, H. & Dutta, P. Structure and phase transitions in Langmuir monolayers. *Rev. Mod. Phys.* **71**, 779–819 (1999).
23. Novoselov, K. S. et al. Electric field effect in atomically thin carbon films. *Science* **306**, 666–669 (2004).
24. Zhang, Y. B., Tan, Y. W., Stormer, H. L. & Kim, P. Experimental observation of the quantum Hall effect and Berry's phase in graphene. *Nature* **438**, 201–204 (2005).
25. Bolotin, K. I., Ghahari, F., Shulman, M. D., Stormer, H. L. & Kim, P. Observation of the fractional quantum Hall effect in graphene. *Nature* **462**, 196–199 (2009).
26. Du, X., Skachko, I., Duerr, F., Luican, A. & Andrei, E. Y. Fractional quantum Hall effect and insulating phase of Dirac electrons in graphene. *Nature* **462**, 192–195 (2009).
27. Cao, Y. et al. Correlated insulator behaviour at half-filling in magic-angle graphene superlattices. *Nature* **556**, 80–84 (2018).
28. Xi, X. X. et al. Ising pairing in superconducting $NbSe_2$ atomic layers. *Nat. Phys.* **12**, 139–143 (2016).
29. Saito, Y., Nojima, T. & Iwasa, Y. Highly crystalline 2D superconductors. *Nat. Rev. Mater.* **2**, 16094 (2017).
30. Cao, Y. et al. Unconventional superconductivity in magic-angle graphene superlattices. *Nature* **556**, 43–50 (2018).
31. Kane, C. L. & Mele, E. J. Quantum spin Hall effect in graphene. *Phys. Rev. Lett.* **95**, 226801 (2005).
32. Konig, M. et al. Quantum spin hall insulator state in HgTe quantum wells. *Science* **318**, 766–770 (2007).
33. Qian, X. F., Liu, J. W., Fu, L. & Li, J. Quantum spin Hall effect in two-dimensional transition metal dichalcogenides. *Science* **346**, 1344–1347 (2014).
This paper predicts that several group 6 transition-metal dichalcogenide monolayers in 1T′ phase are quantum spin Hall insulators competing with the trivial semiconducting 1H phase and metallic 1T phase.
34. Tang, S. J. et al. Quantum spin Hall state in monolayer 1T′-WTe_2. *Nat. Phys.* **13**, 683–687 (2017).
35. Wu, S. F. et al. Observation of the quantum spin Hall effect up to 100 kelvin in a monolayer crystal. *Science* **359**, 76–79 (2018).
36. Chen, G. et al. Tunable correlated Chern insulator and ferromagnetism in a moiré superlattice. *Nature* **579**, 56–61 (2020).
37. Serlin, M. et al. Intrinsic quantized anomalous Hall effect in a moiré heterostructure. *Science* **367**, 900–903 (2020).
38. Polshyn, H. et al. Electrical switching of magnetic order in an orbital Chern insulator. *Nature* **588**, 66–70 (2020).
39. Huang, B. et al. Layer-dependent ferromagnetism in a van der Waals crystal down to the monolayer limit. *Nature* **546**, 270–273 (2017).
The first demonstration that intrinsic ferromagnetism can be present in monolayer CrI_3.
40. Gong, C. et al. Discovery of intrinsic ferromagnetism in two-dimensional van der Waals crystals. *Nature* **546**, 265–269 (2017).
The first demonstration of layer-dependent ferromagnetic transition in 2D $Cr_2Ge_2Te_6$.
41. Burch, K. S., Mandrus, D. & Park, J. G. Magnetism in two-dimensional van der Waals materials. *Nature* **563**, 47–52 (2018).
42. Gong, C. & Zhang, X. Two-dimensional magnetic crystals and emergent heterostructure devices. *Science* **363**, eaav4450 (2019).
43. Gibertini, M., Koperski, M., Morpurgo, A. F. & Novoselov, K. S. Magnetic 2D materials and heterostructures. *Nat. Nanotechnol.* **14**, 408–419 (2019).
44. Mak, K. F., Shan, J. & Ralph, D. C. Probing and controlling magnetic states in 2D layered magnetic materials. *Nat. Rev. Phys.* **1**, 646–661 (2019).
45. Huang, B. et al. Emergent phenomena and proximity effects in two-dimensional magnets and heterostructures. *Nat. Mater.* **19**, 1276–1289 (2020).
46. Eda, G. et al. Coherent atomic and electronic heterostructures of single-layer MoS_2. *ACS Nano* **6**, 7311–7317 (2012).
47. Kappera, R. et al. Phase-engineered low-resistance contacts for ultrathin MoS_2 transistors. *Nat. Mater.* **13**, 1128–1134 (2014).
48. Duerloo, K.-A. N., Li, Y. & Reed, E. J. Structural phase transitions in two-dimensional Mo- and W-dichalcogenide monolayers. *Nat. Commun.* **5**, 4214 (2014).
This paper reports the first comprehensive theoretical study of structural phase transitions in monolayer transition-metal dichalcogenides.
49. Keum, D. H. et al. Bandgap opening in few-layered monoclinic $MoTe_2$. *Nat. Phys.* **11**, 482–486 (2015).
50. Cho, S. et al. Phase patterning for ohmic homojunction contact in $MoTe_2$. *Science* **349**, 625–628 (2015).
51. Wang, Y. et al. Structural phase transition in monolayer $MoTe_2$ driven by electrostatic doping. *Nature* **550**, 487–491 (2017).
52. Zhang, F. et al. Electric-field induced structural transition in vertical $MoTe_2$- and $Mo_{1-x}W_xTe_2$-based resistive memories. *Nat. Mater.* **18**, 55–61 (2019).
53. Sie, E. J. et al. An ultrafast symmetry switch in a Weyl semimetal. *Nature* **565**, 61–66 (2019).
54. Xiao, J. et al. Berry curvature memory through electrically driven stacking transitions. *Nat. Phys.* **16**, 1028–1034 (2020).
The first experimental demonstration of the theoretically predicted ferroelectric nonlinear Hall effect and Berry curvature memory in 2D semimetals.
55. Chang, K. et al. Discovery of robust in-plane ferroelectricity in atomic-thick SnTe. *Science* **353**, 274–278 (2016).
The first experimental report of in-plane ferroelectricity in an atomically thin material.
56. Ding, W. et al. Prediction of intrinsic two-dimensional ferroelectrics in In_2Se_3 and other III_2-VI_3 van der Waals materials. *Nat. Commun.* **8**, 14956 (2017).
The first theoretical prediction of simultaneous out-of-plane and in-plane ferroelectricity in monolayer α-In_2Se_3.
57. Li, W. B. & Li, J. Ferroelasticity and domain physics in two-dimensional transition metal dichalcogenide monolayers. *Nat. Commun.* **7**, 10843 (2016).
One of the earliest studies of ferroelasticity and ferroelastic transitions in 2D materials.
58. Wang, H. & Qian, X. Two-dimensional multiferroics in monolayer group IV monochalcogenides. *2D Mater.* **4**, 015042 (2017).
59. Zhou, J., Xu, H. W., Li, Y. F., Jaramillo, R. & Li, J. Opto-mechanics driven fast martensitic transition in two-dimensional materials. *Nano Lett.* **18**, 7794–7800 (2018).
60. Xu, H., Zhou, J., Li, Y., Jaramillo, R. & Li, J. Optomechanical control of stacking patterns of h-BN bilayer. *Nano Res.* **12**, 2634–2639 (2019).
61. Mishin, Y., Asta, M. & Li, J. Atomistic modeling of interfaces and their impact on microstructure and properties. *Acta Mater.* **58**, 1117–1151 (2010).
62. Mermin, N. D. Crystalline order in two dimensions. *Phys. Rev.* **176**, 250–254 (1968).
63. Splendiani, A. et al. Emerging photoluminescence in monolayer MoS_2. *Nano Lett.* **10**, 1271–1275 (2010).
64. Mak, K. F., Lee, C., Hone, J., Shan, J. & Heinz, T. F. Atomically thin MoS_2: a new direct-gap semiconductor. *Phys. Rev. Lett.* **105**, 136805 (2010).
65. Sohier, T., Gibertini, M., Calandra, M., Mauri, F. & Marzari, N. Breakdown of optical phonons' splitting in two-dimensional materials. *Nano Lett.* **17**, 3758–3763 (2017).
66. Cudazzo, P., Tokatly, I. V. & Rubio, A. Dielectric screening in two-dimensional insulators: implications for excitonic and impurity states in graphane. *Phys. Rev. B* **84**, 085406 (2011).
67. Xi, X. X. et al. Strongly enhanced charge-density-wave order in monolayer $NbSe_2$. *Nat. Nanotechnol.* **10**, 765–769 (2015).
68. Ye, J. T. et al. Superconducting dome in a gate-tuned band insulator. *Science* **338**, 1193–1196 (2012).
69. Li, L. J. et al. Controlling many-body states by the electric-field effect in a two-dimensional material. *Nature* **529**, 185–189 (2016).
70. Fei, Z. Y. et al. Ferroelectric switching of a two-dimensional metal. *Nature* **560**, 336–339 (2018).
71. Yang, Q., Wu, M. & Li, J. Origin of two-dimensional vertical ferroelectricity in WTe_2 bilayer and multilayer. *J. Phys. Chem. Lett.* **9**, 7160–7164 (2018).
72. Feng, J., Qi, L., Huang, J. Y. & Li, J. Geometric and electronic structure of graphene bilayer edges. *Phys. Rev. B* **80**, 165407 (2009).
73. Kushima, A., Qian, X. F., Zhao, P., Zhang, S. L. & Li, J. Ripplocations in van der Waals layers. *Nano Lett.* **15**, 1302–1308 (2015).
74. Britnell, L. et al. Strong light-matter interactions in heterostructures of atomically thin films. *Science* **340**, 1311–1314 (2013).
75. Elias, D. C. et al. Control of graphene's properties by reversible hydrogenation: evidence for graphane. *Science* **323**, 610–613 (2009).
76. Lin, Y. C., Dumcencon, D. O., Huang, Y. S. & Suenaga, K. Atomic mechanism of the semiconducting-to-metallic phase transition in single-layered MoS_2. *Nat. Nanotechnol.* **9**, 391–396 (2014).
77. Franklin, B. Of the stilling of waves by means of oil. *Philos. Trans. R. Soc. Lond.* **64**, 445–460 (1774).
78. Lord Rayleigh Measurements of the amount of oil necessary in order to check the motions of camphor upon water. *Proc. R. Soc. Lond.* **47**, 364–367 (1890).
79. Nair, R. R. et al. Fine structure constant defines visual transparency of graphene. *Science* **320**, 1308–1308 (2008).
80. Rehn, D. A., Li, Y., Pop, E. & Reed, E. J. Theoretical potential for low energy consumption phase change memory utilizing electrostatically-induced structural phase transitions in 2D materials. *NPJ Comput. Mater.* **4**, 2 (2018).
81. Simpson, R. E. et al. Interfacial phase-change memory. *Nat. Nanotechnol.* **6**, 501–505 (2011).
82. Gu, X. K., Wei, Y. J., Yin, X. B., Li, B. W. & Yang, R. G. Colloquium: Phononic thermal properties of two-dimensional materials. *Rev. Mod. Phys.* **90**, 041002 (2018).
83. Li, J. The mechanics and physics of defect nucleation. *MRS Bull.* **32**, 151–159 (2007).
84. Zhu, T. & Li, J. Ultra-strength materials. *Prog. Mater. Sci.* **55**, 710–757 (2010).
85. Yakobson, B. I. Mechanical relaxation and "intramolecular plasticity" in carbon nanotubes. *Appl. Phys. Lett.* **72**, 918–920 (1998).
86. Lee, C., Wei, X., Kysar, J. W. & Hone, J. Measurement of the elastic properties and intrinsic strength of monolayer graphene. *Science* **321**, 385–388 (2008).
87. Bertolazzi, S., Brivio, J. & Kis, A. Stretching and breaking of ultrathin MoS_2. *ACS Nano* **5**, 9703–9709 (2011).
88. Li, J., Shan, Z. W. & Ma, E. Elastic strain engineering for unprecedented materials properties. *MRS Bull.* **39**, 108–117 (2014).
89. Song, S. et al. Room temperature semiconductor–metal transition of $MoTe_2$ thin films engineered by strain. *Nano Lett.* **16**, 188–193 (2015).
90. Hou, W. et al. Strain-based room-temperature non-volatile $MoTe_2$ ferroelectric phase change transistor. *Nat. Nanotechnol.* **14**, 668–673 (2019).
91. Bausch, A. R. et al. Grain boundary scars and spherical crystallography. *Science* **299**, 1716–1718 (2003).
92. Masel, R. I. *Principles of Adsorption and Reaction on Solid Surfaces* (Wiley, 1996).
93. Geim, A. K. & Grigorieva, I. V. Van der Waals heterostructures. *Nature* **499**, 419–425 (2013).
94. Jones, D. A. *Principles and Prevention of Corrosion* 2nd edn (Prentice Hall, 1996).
95. Dean, C. R. et al. Boron nitride substrates for high-quality graphene electronics. *Nat. Nanotechnol.* **5**, 722–726 (2010).
This work shows that hexagonal boron nitride is an excellent material for protecting the properties of 2D materials.
96. Nine, M. J., Cole, M. A., Tran, D. N. H. & Losic, D. Graphene: a multipurpose material for protective coatings. *J. Mater. Chem. A* **3**, 12580–12602 (2015).
97. Su, C. et al. Waterproof molecular monolayers stabilize 2D materials. *Proc. Natl Acad. Sci. USA* **116**, 20844–20849 (2019).
98. Levy, N. et al. Strain-induced pseudo-magnetic fields greater than 300 tesla in graphene nanobubbles. *Science* **329**, 544–547 (2010).
99. Feng, J., Qian, X. F., Huang, C. W. & Li, J. Strain-engineered artificial atom as a broad-spectrum solar energy funnel. *Nat. Photonics* **6**, 865–871 (2012).
100. Voiry, D. et al. Enhanced catalytic activity in strained chemically exfoliated WS_2 nanosheets for hydrogen evolution. *Nat. Mater.* **12**, 850–855 (2013).
101. Voiry, D., Mohite, A. & Chhowalla, M. Phase engineering of transition metal dichalcogenides. *Chem. Soc. Rev.* **44**, 2702–2712 (2015).
102. Wang, J., Wei, Y., Li, H., Huang, X. & Zhang, H. Crystal phase control in two-dimensional materials. *Sci. China Chem.* **61**, 1227–1242 (2018).
103. Xiao, Y., Zhou, M., Liu, J., Xu, J. & Fu, L. Phase engineering of two-dimensional transition metal dichalcogenides. *Sci. China Mater.* **62**, 759–775 (2019).

104. Wang, X. et al. Potential 2D materials with phase transitions: structure, synthesis, and device applications. *Adv. Mater.* **31**, 1804682 (2019).
105. Sokolikova, M. S. & Mattevi, C. Direct synthesis of metastable phases of 2D transition metal dichalcogenides. *Chem. Soc. Rev.* **49**, 3952–5980 (2020).
106. Bergeron, H., Lebedev, D. & Hersam, M. C. Polymorphism in post-dichalcogenide two-dimensional materials. *Chem. Rev.* **121**, 2713–2775 (2021).
107. Wilson, J. A. & Yoffe, A. D. The transition metal dichalcogenides discussion and interpretation of the observed optical, electrical and structural properties. *Adv. Phys.* **18**, 193–335 (1969).
108. Xia, F., Wang, H., Xiao, D., Dubey, M. & Ramasubramaniam, A. Two-dimensional material nanophotonics. *Nat. Photonics* **8**, 899–907 (2014).
109. Fei, Z. et al. Edge conduction in monolayer WTe_2. *Nat. Phys.* **13**, 677–682 (2017).
110. Zheng, F. et al. On the quantum spin Hall gap of monolayer 1T′-WTe_2. *Adv. Mater.* **28**, 4845–4851 (2016).
111. Sajadi, E. et al. Gate-induced superconductivity in a monolayer topological insulator. *Science* **362**, 922–925 (2018).
112. Duerloo, K.-A. N. & Reed, E. J. Structural phase transitions by design in monolayer alloys. *ACS Nano* **10**, 289–297 (2015).
113. Li, Y., Duerloo, K.-A. N., Wauson, K. & Reed, E. J. Structural semiconductor-to-semimetal phase transition in two-dimensional materials induced by electrostatic gating. *Nat. Commun.* **7**, 10671 (2016).
114. Py, M. A. & Haering, R. R. Structural destabilization induced by lithium intercalation in MoS_2 and related compounds. *Can. J. Phys.* **61**, 76–84 (1983).
115. Gordon, R. A., Yang, D., Crozier, E. D., Jiang, D. T. & Frindt, R. F. Structures of exfoliated single layers of WS_2, MoS_2, and $MoSe_2$ in aqueous suspension. *Phys. Rev. B* **65**, 125407 (2002).
116. Chhowalla, M. et al. The chemistry of two-dimensional layered transition metal dichalcogenide nanosheets. *Nat. Chem.* **5**, 263–275 (2013).
117. Wadhawan, V. K. *Introduction to Ferroic Materials* (Gordon & Breach, 2000).
118. Wang, G.-Y. et al. Formation mechanism of twin domain boundary in 2D materials: The case for WTe_2. *Nano Res.* **12**, 569–573 (2019).
119. Pedramrazi, Z. et al. Manipulating topological domain boundaries in the single-layer quantum spin Hall insulator 1T′–WSe_2. *Nano Lett.* **19**, 5634–5639 (2019).
120. Kim, H. W. et al. Symmetry dictated grain boundary state in a two-dimensional topological insulator. *Nano Lett.* **20**, 5837–5843 (2020).
121. Seixas, L., Rodin, A. S., Carvalho, A. & Castro Neto, A. H. Multiferroic two-dimensional materials. *Phys. Rev. Lett.* **116**, 206803 (2016).
122. Dawber, M., Rabe, K. M. & Scott, J. F. Physics of thin-film ferroelectric oxides. *Rev. Mod. Phys.* **77**, 1083–1130 (2005).
123. Ahn, C. H., Rabe, K. M. & Triscone, J.-M. Ferroelectricity at the nanoscale: local polarization in oxide thin films and heterostructures. *Science* **303**, 488–491 (2004).
124. Wu, M. & Zeng, X. C. Intrinsic ferroelasticity and/or multiferroicity in two-dimensional phosphorene and phosphorene analogues. *Nano Lett.* **16**, 3236–3241 (2016).
125. Fei, R., Kang, W. & Yang, L. Ferroelectricity and phase transitions in monolayer group-IV monochalcogenides. *Phys. Rev. Lett.* **117**, 097601 (2016).
126. Hanakata, P. Z., Carvalho, A., Campbell, D. K. & Park, H. S. Polarization and valley switching in monolayer group-IV monochalcogenides. *Phys. Rev. B* **94**, 035304 (2016).
127. Mehboudi, M. et al. Structural phase transition and material properties of few-layer monochalcogenides. *Phys. Rev. Lett.* **117**, 246802 (2016).
128. Mehboudi, M. et al. Two-dimensional disorder in black phosphorus and monochalcogenide monolayers. *Nano Lett.* **16**, 1704–1712 (2016).
129. Zhou, Y. et al. Out-of-plane piezoelectricity and ferroelectricity in layered α-In_2Se_3 nanoflakes. *Nano Lett.* **17**, 5508–5513 (2017).
130. Cui, C. et al. Intercorrelated in-plane and out-of-plane ferroelectricity in ultrathin two-dimensional layered semiconductor In_2Se_3. *Nano Lett.* **18**, 1253–1258 (2018).
131. Xiao, J. et al. Intrinsic two-dimensional ferroelectricity with dipole locking. *Phys. Rev. Lett.* **120**, 227601 (2018).
132. Zheng, C. et al. Room temperature in-plane ferroelectricity in van der Waals In_2Se_3. *Sci. Adv.* **4**, eaar7720 (2018).
133. Belianinov, A. et al. $CuInP_2S_6$ room temperature layered ferroelectric. *Nano Lett.* **15**, 3808–3814 (2015).
134. Liu, F. et al. Room-temperature ferroelectricity in $CuInP_2S_6$ ultrathin flakes. *Nat. Commun.* **7**, 12357 (2016).
135. Yuan, S. et al. Room-temperature ferroelectricity in $MoTe_2$ down to the atomic monolayer limit. *Nat. Commun.* **10**, 1775 (2019).
136. Shirodkar, S. N. & Waghmare, U. V. Emergence of ferroelectricity at a metal-semiconductor transition in a 1T monolayer of MoS_2. *Phys. Rev. Lett.* **112**, 157601 (2014).
137. Soluyanov, A. A. et al. Type-II Weyl semimetals. *Nature* **527**, 495–498 (2015).
138. Brown, B. E. The crystal structures of WTe_2 and high-temperature $MoTe_2$. *Acta Crystallogr.* **20**, 268–274 (1966).
139. Cochran, W. Crystal stability and the theory of ferroelectricity. *Adv. Phys.* **9**, 387–423 (1960).
140. Wang, H. & Qian, X. Ferroelectric nonlinear anomalous Hall effect in few-layer WTe_2. *NPJ Comput. Mater.* **5**, 119 (2019).
141. Herring, C. & Kittel, C. On the theory of spin waves in ferromagnetic media. *Phys. Rev.* **81**, 869–880 (1951).
142. Fröhlich, J. & Lieb, E. H. Existence of phase transitions for anisotropic Heisenberg models. *Phys. Rev. Lett.* **38**, 440–442 (1977).
143. Li, W. et al. High temperature ferromagnetism in π-conjugated two-dimensional metal–organic frameworks. *Chem. Sci.* **8**, 2859–2867 (2017).
144. Wang, H., Qi, J. & Qian, X. Electrically tunable high Curie temperature two-dimensional ferromagnetism in van der Waals layered crystals. *Appl. Phys. Lett.* **117**, 083102 (2020).
145. Jiang, Z., Wang, P., Xing, J., Jiang, X. & Zhao, J. Screening and design of novel 2D ferromagnetic materials with high Curie temperature above room temperature. *ACS Appl. Mater. Interfaces* **10**, 39032–39039 (2018).
146. Telford, E. J. et al. layered antiferromagnetism induces large negative magnetoresistance in the van der Waals semiconductor CrSBr. *Adv. Mater.* **32**, 2003240 (2020).
147. Lee, K. et al. Magnetic order and symmetry in the 2D semiconductor CrSBr. Preprint at *arXiv* https://arxiv.org/abs/2007.10715 (2020).
148. Zhuang, H. L., Kent, P. R. C. & Hennig, R. G. Strong anisotropy and magnetostriction in the two-dimensional Stoner ferromagnet Fe_3GeTe_2. *Phys. Rev. B* **93**, 134407 (2016).
149. Deng, Y. et al. Gate-tunable room-temperature ferromagnetism in two-dimensional Fe_3GeTe_2. *Nature* **563**, 94–99 (2018).
150. Bogaert, K. et al. Diffusion-mediated synthesis of MoS_2/WS_2 lateral heterostructures. *Nano Lett.* **16**, 5129–5134 (2016).
151. Zhou, J. et al. A library of atomically thin metal chalcogenides. *Nature* **556**, 355–359 (2018).
152. Li, X. et al. Surfactant-mediated growth and patterning of atomically thin transition metal dichalcogenides. *ACS Nano* **6**, 6570–6581 (2020).
153. Zhu, J. et al. Argon plasma induced phase transition in monolayer MoS_2. *J. Am. Chem. Soc.* **139**, 10216–10219 (2017).
154. Zhou, L. et al. Large-area synthesis of high-quality uniform few-layer $MoTe_2$. *J. Am. Chem. Soc.* **137**, 11892–11895 (2015).
155. Liu, L. N. et al. Phase-selective synthesis of 1T′ MoS_2 monolayers and heterophase bilayers. *Nat. Mater.* **17**, 1108–1114 (2018).
156. Rao, F. et al. Reducing the stochasticity of crystal nucleation to enable subnanosecond memory writing. *Science* **358**, 1423–1426 (2017).
157. Zhang, W., Mazzarello, R., Wuttig, M. & Ma, E. Designing crystallization in phase-change materials for universal memory and neuro-inspired computing. *Nat. Rev. Mater.* **4**, 150–168 (2019).
158. Kalikka, J. et al. Strain-engineered diffusive atomic switching in two-dimensional crystals. *Nat. Commun.* **7**, 11983 (2016).
159. Ding, K. et al. Phase-change heterostructure enables ultralow noise and drift for memory operation. *Science* **366**, 210–215 (2019).
160. Wu, J. et al. High tunnelling electroresistance in a ferroelectric van der Waals heterojunction via giant barrier height modulation. *Nat. Electron.* **3**, 466–472 (2020).
161. Shi, G. & Kioupakis, E. Anisotropic spin transport and strong visible-light absorbance in few-layer SnSe and GeSe. *Nano Lett.* **15**, 6926–6931 (2015).
162. Zhu, X. J., Li, D., Liang, X. G. & Lu, W. D. Ionic modulation and ionic coupling effects in MoS_2 devices for neuromorphic computing. *Nat. Mater.* **18**, 141–148 (2019).
163. Zhang, X. et al. Two-dimensional MoS_2-enabled flexible rectenna for Wi-Fi-band wireless energy harvesting. *Nature* **566**, 368–372 (2019).
164. Wang, H. & Qian, X. Ferroicity-driven nonlinear photocurrent switching in time-reversal invariant ferroic materials. *Sci. Adv.* **5**, eaav9743 (2019).
165. Peng, B. et al. Phase transition enhanced superior elasticity in freestanding single-crystalline multiferroic $BiFeO_3$ membranes. *Sci. Adv.* **6**, eaba5847 (2020).
166. Jiang, S., Xie, H., Shan, J. & Mak, K. F. Exchange magnetostriction in two-dimensional antiferromagnets. *Nat. Mater.* **19**, 1295–1299 (2020).
167. Oganov, A. R., Pickard, C. J., Zhu, Q. & Needs, R. J. Structure prediction drives materials discovery. *Nat. Rev. Mater.* **4**, 331–348 (2019).
168. Butler, K. T., Davies, D. W., Cartwright, H., Isayev, O. & Walsh, A. Machine learning for molecular and materials science. *Nature* **559**, 547–555 (2018).
169. Schmidt, J., Marques, M. R. G., Botti, S. & Marques, M. A. L. Recent advances and applications of machine learning in solid-state materials science. *NPJ Comput. Mater.* **5**, 83 (2019).
170. Cheon, G. et al. Revealing the spectrum of unknown layered materials with superhuman predictive abilities. *J. Phys. Chem. Lett.* **9**, 6967–6972 (2018).
171. Oses, C., Toher, C. & Curtarolo, S. High-entropy ceramics. *Nat. Rev. Mater.* **5**, 295–309 (2020).
172. Souvatzis, P., Eriksson, O., Katsnelson, M. I. & Rudin, S. P. Entropy driven stabilization of energetically unstable crystal structures explained from first principles theory. *Phys. Rev. Lett.* **100**, 095901 (2008).
173. Lebègue, S., Björkman, T., Klintenberg, M., Nieminen, R. M. & Eriksson, O. Two-dimensional materials from data filtering and ab initio calculations. *Phys. Rev. X* **3**, 031002 (2013).
174. Ashton, M., Paul, J., Sinnott, S. B. & Hennig, R. G. Topology-scaling identification of layered solids and stable exfoliated 2D materials. *Phys. Rev. Lett.* **118**, 106101 (2017).
175. Cheon, G. et al. Data mining for new two- and one-dimensional weakly bonded solids and lattice-commensurate heterostructures. *Nano Lett.* **17**, 1915–1923 (2017).
176. Mounet, N. et al. Two-dimensional materials from high-throughput computational exfoliation of experimentally known compounds. *Nat. Nanotechnol.* **13**, 246–252 (2018).
177. Haastrup, S. et al. The computational 2D materials database: high-throughput modeling and discovery of atomically thin crystals. *2D Mater.* **5**, 042002 (2018).
178. Taheri, M. L. et al. Current status and future directions for in situ transmission electron microscopy. *Ultramicroscopy* **170**, 86–95 (2016).
179. Lindenberg, A. M., Johnson, S. L. & Reis, D. A. Visualization of atomic-scale motions in materials via femtosecond X-ray scattering techniques. *Annu. Rev. Mater. Res.* **47**, 425–449 (2017).
180. Sciaini, G. & Miller, R. J. D. Femtosecond electron diffraction: heralding the era of atomically resolved dynamics. *Rep. Prog. Phys.* **74**, 096101 (2011).
181. Bovensiepen, U. & Kirchmann, P. S. Elementary relaxation processes investigated by femtosecond photoelectron spectroscopy of two-dimensional materials. *Laser Photonics Rev.* **6**, 589–606 (2012).
182. Raschke, M. B. & Shen, Y. R. Nonlinear optical spectroscopy of solid interfaces. *Curr. Opin. Solid State Mater. Sci.* **8**, 343–352 (2004).
183. Danz, T., Domröse, T. & Ropers, C. Ultrafast nanoimaging of the order parameter in a structural phase transition. *Science* **371**, 371–374 (2021).
184. Huang, P. Y. et al. Grains and grain boundaries in single-layer graphene atomic patchwork quilts. *Nature* **469**, 389–392 (2011).
185. Fasolino, A., Los, J. H. & Katsnelson, M. I. Intrinsic ripples in graphene. *Nat. Mater.* **6**, 858–861 (2007).
186. McGilly, L. J. et al. Visualization of moiré superlattices. *Nat. Nanotechnol.* **15**, 580–584 (2020).
187. Kim, H.-J., Kang, S.-H., Hamada, I. & Son, Y.-W. Origins of the structural phase transitions in

$MoTe_2$ and WTe_2. *Phys. Rev. B* **95**, 180101(R) (2017).
188. Bistritzer, R. & MacDonald, A. H. Moiré bands in twisted double-layer graphene. *Proc. Natl Acad. Sci. USA* **108**, 12233–12237 (2011).
This paper predicts the existence of strong-correlation physics in magic-angle twisted bilayer graphene.
189. Balents, L., Dean, C. R., Efetov, D. K. & Young, A. F. Superconductivity and strong correlations in moiré flat bands. *Nat. Phys.* **16**, 725–733 (2020).
190. Qian, X., Wang, Y., Li, W., Lu, J. & Li, J. Modelling of stacked 2D materials and devices. *2D Mater.* **2**, 032003 (2015).
191. Wang, H. & Qian, X. Electrically and magnetically switchable nonlinear photocurrent in *PT*-symmetric magnetic topological quantum materials. *NPJ Comput. Mater.* **6**, 199 (2020).
192. Salén, P. et al. Matter manipulation with extreme terahertz light: Progress in the enabling THz technology. *Phys. Rep.* **836–837**, 1–74 (2019).
193. Carr, S., Fang, S. & Kaxiras, E. Electronic-structure methods for twisted moiré layers. *Nat. Rev. Mater.* **5**, 748–763 (2020).
194. Andrei, E. Y. & MacDonald, A. H. Graphene bilayers with a twist. *Nat. Mater.* **19**, 1265–1275 (2020).
195. Kennes, D. M. et al. Moiré heterostructures as a condensed-matter quantum simulator. *Nat. Phys.* **17**, 155–163 (2021).
196. IEEE. *International Roadmap for Devices and Systems: 2020 Edition* (IEEE, 2020).
197. Baxter, R. J. Eight-vertex model in lattice statistics. *Phys. Rev. Lett.* **26**, 832–833 (1971).
198. Halperin, B. I. & Nelson, D. R. Theory of two-dimensional melting. *Phys. Rev. Lett.* **41**, 121–124 (1978).
199. Young, A. P. Melting and the vector Coulomb gas in two dimensions. *Phys. Rev. B* **19**, 1855–1866 (1979).
200. Nelson, D. R. & Halperin, B. I. Dislocation-mediated melting in two dimensions. *Phys. Rev. B* **19**, 2457–2484 (1979).
201. Thouless, D. J., Kohmoto, M., Nightingale, M. P. & den Nijs M. Quantized Hall conductance in a two-dimensional periodic potential. *Phys. Rev. Lett.* **49**, 405–408 (1982).
202. Laughlin, R. B. Anomalous quantum Hall effect: An incompressible quantum fluid with fractionally charged excitations. *Phys. Rev. Lett.* **50**, 1395–1398 (1983).
203. Bednorz, J. G. & Müller, K. A. Possible high T_c superconductivity in the Ba–La–Cu–O system. *Z. Phys. B Condens. Matter* **64**, 189–193 (1986).
204. Kantor, Y. & Nelson, D. R. Crumpling transition in polymerized membranes. *Phys. Rev. Lett.* **58**, 2774–2777 (1987).
205. Kane, C. L. & Mele, E. J. $Z(2)$ topological order and the quantum spin Hall effect. *Phys. Rev. Lett.* **95**, 146802 (2005).
206. Mayorov, A. S. et al. Micrometer-scale ballistic transport in encapsulated graphene at room temperature. *Nano Lett.* **11**, 2396–2399 (2011).
207. Rehn, D. A. & Reed, E. J. Memristors with distorted structures. *Nat. Mater.* **18**, 8–9 (2019).

Acknowledgements
J.L. acknowledges support by NSF DMR-1923976. X.Q. acknowledges support by NSF DMR-1753054. W.L. is grateful for the support by NSFC under project no. 62004172, Westlake Multidisciplinary Research Initiative Center (MRIC) under award no. 20200101 and Westlake University HPC Center. We thank the anonymous reviewers for their valuable comments and suggestions.

Author contributions
J.L. conceived the framework of the Review. All authors researched data for the article, discussed the content and contributed to the writing and revising of the manuscript.

Competing interests
The authors declare no competing interests.

Publisher's note
Springer Nature remains neutral with regard to jurisdictional claims in published maps and institutional affiliations.